

# 1 Reconstructing hydroclimate changes of past 2,500 years 2 using speleothems from Pyrenean caves (NE Spain)

3 Miguel Bartolomé<sup>1,2,3\*</sup>, Ana Moreno<sup>4\*</sup>, Carlos Sancho<sup>5†</sup>, Isabel Cacho<sup>6</sup>, Heather Stoll<sup>3</sup>,  
4 Negar Haghpor<sup>3,7</sup>, Ánchel Belmonte<sup>8</sup>, Christoph Spötl<sup>9</sup>, John Hellstrom<sup>10</sup>, R. Lawrence  
5 Edwards<sup>11</sup> and Hai Cheng<sup>12,13,14</sup>

6 <sup>1</sup> Departamento de Geología. Museo Nacional de Ciencias Naturales (CSIC). C. de José Gutiérrez  
7 Abascal, 2, 28006 Madrid, Spain.

8 <sup>2</sup> Swiss Institute for Speleology and Karst Studies (SISKA), Rue de la Serre 68 2300 La Chaux-de-Fonds,  
9 Switzerland.

10 <sup>3</sup> Geological Institute, NO G59, Department of Earth Sciences, Sonneggstrasse 5, ETH, 8092 Zurich,  
11 Switzerland.

12 <sup>4</sup> Department of Geoenvironmental Processes and Global Change, Pyrenean Institute of Ecology (IPE-  
13 CSIC), Avda. Montañana 1005, 50059 Zaragoza, Spain.

14 <sup>5†</sup> Earth Sciences Department, University of Zaragoza, C/Pedro Cerbuna 12, 50009 Zaragoza, Spain.  
15 Deceased.

16 <sup>6</sup> CRG Geociències Marines, Dept. Dinàmica de la Terra i de l'Oceà, Universitat de Barcelona, 08028  
17 Barcelona, Spain

18 <sup>7</sup> Laboratory for Ion Beam Physics, Department of Physics, ETH Zurich, Switzerland

19 <sup>8</sup> Sobrarbe-Pirineos UNESCO Global Geopark. Boltaña. Spain.

20 <sup>9</sup> Institute of Geology, University of Innsbruck, 6020, Innsbruck, Austria

21 <sup>10</sup> School of Earth Sciences, The University of Melbourne, VIC 3010, Australia

22 <sup>11</sup> Department of Earth and Environmental Sciences, University of Minnesota, Minneapolis, MN, 55455,  
23 USA

24 <sup>12</sup> Institute of Global Environmental Change, Xi'an Jiaotong University, Xi'an, 710049, China.

25 <sup>13</sup> State Key Laboratory of Loess and Quaternary Geology, Institute of Earth Environment, 11 Chinese  
26 Academy of Sciences, Xi'an, 710061, China.

27 <sup>14</sup> Key Laboratory of Karst Dynamics, MLR, Institute of Karst Geology, CAGS, Guilin, 541004, China.

28  
29 \* Both authors have contributed equally to this manuscript

30 *Corresponding author:* Ana Moreno ([amoreno@ipe.csic.es](mailto:amoreno@ipe.csic.es))

31  
32 **Abstract.** Reconstructing of past hydroclimates at regional scales during the Common Era (CE) is  
33 necessary to place the current warming in the context of natural climate variability. Here we present a  
34 composite record of oxygen isotope variations during last 2500 years based on eight stalagmites from four  
35 caves in the central Pyrenees (NE Spain) dominated by temperature variations, with amount of precipitation  
36 playing a minor role. The dataset is compared with other Iberian reconstructions that show a high degree  
37 of internal coherence with respect to variability at the centennial scale. The Roman Period (RP) (especially  
38 0-200 CE), the Medieval Climate Anomaly (MCA), and part of the Little Ice Age (LIA) represent the  
39 warmest periods, while the coldest decades occurred during the Dark Ages (DA) and most of the LIA  
40 intervals (e.g., 520-550 CE and 1800-1850 CE). Importantly, the LIA cooling or the MCA warming were  
41 not continuous or uniform and exhibited high decadal variability. The Industrial Era (IE) shows an overall  
42 warming trend although with marked cycles and partial stabilization during the last two decades (1990-  
43 2010). The strong coherence between the speleothem data, European temperature reconstructions and  
44 global tree-ring data informs about the regional representativeness of this new record as Pyrenean past  
45 climate variations. Solar variability, likely through its impact on the North Atlantic Oscillation, and major  
46 volcanic eruptions appear to be the two main drivers of climate in southwestern Europe during the past 2.5  
47 millennia.

48 **Keywords.** Iberian Peninsula, Central Pyrenees, late Holocene, stalagmite, temperature reconstruction

## 49 1. Introduction

50 Global surface temperatures in the first two decades of the 21<sup>st</sup> century (2001–2020) were 0.84 to 1.10 °C  
51 warmer than 1850–1900 CE (IPCC, 2021). There is strong evidence that anthropogenic global warming is  
52 unprecedented in terms of absolute temperatures and spatial consistency over the past 2000 yr (Ahmed et  
53 al., 2013; Konecky et al., 2020). On the contrary, pre-industrial temperatures were less spatially coherent,  
54 and further work is needed to explain the regional expression of climate change (Mann, 2021; Neukom et  
55 al., 2019). Obtaining new and high-quality records in terms of resolution, dating and regional  
56 representativeness is thus critical for characterizing natural climate variability on decadal to centennial  
57 scales (PAGES2k Consortium et al., 2017).

58 High mountains are particularly sensitive regions to climate change and among them the Pyrenees occupy  
59 a crucial frontier position in southern Europe, influenced by both Mediterranean and Atlantic climates. In  
60 the Pyrenees, the temperature has increased by more than 1.5°C since 1882, as shown by the longest time  
61 series from the Pic du Midi observatory (Bücher and Dessens, 1991; Dessens and Bücher, 1995). Recent  
62 studies confirm this warming trend, showing an increase of 0.1 °C per decade during the last century in  
63 Central Pyrenees (Pérez-Zanón et al., 2017), or even 0.28°C per decade if only the 1959-2015 period is  
64 considered (Observatorio Pirenaico de Cambio Global, 2018). Long-term snow depth observations (starting  
65 in 1955) show a statistically significant decline, especially at elevations above 2000 m a.s.l. (López-Moreno  
66 et al., 2020). This fact, together with the increase in temperature, has caused the glaciated area in the  
67 Pyrenees to decrease by 21.9% in the last decade (Vidaller et al., 2021), changing from 2060 ha during the  
68 LIA to 242 ha in 2016 (Rico et al., 2017). Recent studies on one of the emblematic glaciers in the Pyrenees,  
69 the Monte Perdido glacier, show that the current ice retreat is unprecedented in the last 2000 years, as this  
70 glacier survived previous warm periods such as the MCA and the RP (Moreno et al., 2021b).

71 The study of sediment records from lakes in the Pyrenees, where considerable variations in water level,  
72 water chemistry, and biological processes have occurred due to changes in effective moisture and  
73 temperature, is an excellent approach to reconstruct past climate variability (González-Sampérez et al.,  
74 2017). Recently, a comprehensive study in six high altitude Pyrenean lakes indicates unprecedented  
75 changes in the lithogenic and organic carbon fluxes since 1950 CE, suggesting an increase in algal  
76 productivity likely favoured by warmer temperatures and higher nutrient deposition associated to the Great  
77 Acceleration (Vicente de Vera García et al., 2023), a period when human-driven global, social,  
78 technological, and environmental changes intensifying dramatically (Steffen et al., 2015). Marine records  
79 off the Iberian coast show a clear long-term cooling trend, from 0 CE to the beginning of the 20th century,  
80 probably reflecting the decline in Northern Hemisphere summer insolation that began after the Holocene  
81 optimum (Abrantes et al., 2017). Unfortunately, it is not possible to record decadal temperature changes  
82 from the studied proxies of these lake or marine records, so other archives allowing higher chronological  
83 robustness and larger resolution are required.

84 The Central Pyrenees are largely composed of limestones and host numerous caves, some of which are rich  
85 in speleothems, thus making it possible to reconstruct the past climate by studying stalagmites from  
86 different caves. Unfortunately, despite the high potential of stalagmite with annually to sub-annual  
87 resolution in the CE, it is extremely difficult to obtain high-resolution and well-replicated records. In most  
88 cases, the CE period spans only a few centimetres, limiting the number of samples drilled for high-precision  
89 U-Th dating (PAGES Hydro2k Consortium, 2017). In addition to this chronological challenge, the  
90 interpretation of oxygen isotopes of speleothems ( $\delta^{18}\text{O}_c$ ) from southern Europe is also complex (Moreno et  
91 al., 2021a). Recent studies of Pyrenean stalagmites covering the last deglaciation indicate the important  
92 role of changes in annual temperature in the variability of  $\delta^{18}\text{O}_c$  (Bartolomé et al., 2015a; Bernal-Wormull  
93 et al., 2021). However, correct interpretation of  $\delta^{18}\text{O}_c$  proxies requires a sound understanding of the  
94 influence of climate variables on carbonate deposition in caves through monitoring (e.g. Pérez-Mejías et  
95 al., 2018) and calibration to the instrumental period (Mangini et al., 2005; Tadros et al., 2022).

96 In this study, we provide high-resolution  $\delta^{18}\text{O}_c$  data for eight stalagmites from four different caves in the  
97 Central Pyrenees, allowing us to construct a stacked curve of climate variability for the last 2500 years with

98 potential regional representativeness. These eight stalagmites allow climate changes during the CE to be  
99 studied in reasonably robust chronological framework. Monitoring and calibration of  $\delta^{18}\text{O}_c$  with  
100 instrumental data for the two youngest stalagmites suggests that the  $\delta^{18}\text{O}_c$  variability primarily reflects  
101 annual temperatures, while precipitation (eg. amount of precipitation, seasonality, source) played a role  
102 during certain periods. This new record represents an excellent opportunity to characterize natural  
103 temperature changes in this region on decadal to centennial scales for the last 2500 years and compare them  
104 with other approaches to examine their regional representativeness.

## 105 **2. Study sites**

### 106 **2.1. Geological setting, climate and vegetation**

107 This study of speleothems is located in the central sector of the Pyrenees, in northeastern Iberia (Fig. 1a,b).  
108 All caves are located in the Sobrarbe Geopark, close to or at the borders of the Ordesa and Monte Perdido  
109 National Park, formed in Mesozoic and Cenozoic limestones and at different altitudes (Fig. 1c). This area  
110 has a steep topography due to the high altitudinal gradient and constitutes the largest limestone massif in  
111 Europe (with 22 peaks above 3000 m a.s.l.).

112 The climate is Mediterranean according to the Köppen classification. However, the high relief influences  
113 the climate of this high-altitude area which is accurately described as humid sub-Mediterranean because of  
114 higher rainfall than the typically Mediterranean climate, particularly for the caves above 1000 m a.s.l. where  
115 annual precipitation is above 1000-1200mm and falls mostly as snow. In lower altitude caves (e.g. Seso  
116 Cave) mean annual precipitation is 900 mm, concentrated in spring and fall. Mean air temperatures range  
117 from 0.5 to 15°C, depending on the altitude.

118 Around the caves, in the valleys, there are mid-mountain forests dominated by *Pinus sylvestris* and *Quercus*  
119 *ilex*, as well as shrublands, whereas the highlands are characterized by exposed rock with sparse vegetation  
120 such as meadows.

### 121 **2.2. Cave locations**

122 Seso cave (42°27'23.08"N; 0°02'23.18"E, 794 m a.s.l.) is formed in the eastern flank of the Boltaña  
123 Anticline, close to Boltaña village. The cave developed in insoluble marly strata between limestone beds  
124 of Eocene age. The cave system consists of two longitudinal shallow galleries (2-3m of limestone thickness  
125 over the cave) controlled by the bedding and the main set of joints. Formation of this shallow cave involved  
126 the mechanical removal of large amounts of marl under vadose conditions which took place about 60-40  
127 ka BP (Bartolomé et al., 2015b). Subsequently, calcite speleothems formed which became more abundant  
128 during the Holocene. Average annual temperature inside Seso cave is ~11.8°C.

129 Las Gloces cave (42°35'40" N, 0°1'41"W, 1243 m a.s.l.) is located on the border of the Ordesa National  
130 Park, next to Fanlo village. The cave formed in limestones of Early Eocene age. The limestone's thickness  
131 above the cave is ~20-30 m. Two galleries form the cave. The upper one preserves phreatic features and  
132 hosts the majority of speleothems located in a small room, while vadose morphologies characterize the  
133 lower gallery. Average annual temperature where the stalagmites were taken is ~ 9.8 °C

134 B-1 cave (42°36'0.2"N; 0°7'46"E; 1090 m a.s.l.) is the lower entrance of the Las Fuentes de Escuaín  
135 karstic system, and acts as the collector of all water drained by the system. This system comprises more  
136 than 40 km of galleries and shows a vertical extension of -1150 m. It drains an area of ~15 km<sup>2</sup> and  
137 developed mostly in Eocene limestones. Since a river runs through the cave, several detrital sequences  
138 appear, as well as speleothems, affected by floods. The cave is then well ventilated and shows annual  
139 temperature variations in response to the seasonal ventilation changes and seasonal flooding. The studied  
140 sample was obtained in a fossil gallery, not currently influenced by flooding and with an average annual  
141 temperature of ~9.5°C.

142 Pot au Feu cave (42°31.48' N; 0°14.26' W; 996 m a.s.l.) is located in the Irués river valley in the Cotiella  
143 massif. The host rock is an Upper Cretaceous limestone. Hydrogeologically, the cave belongs to the high  
144 mountain unconfined karst Cotiella-Turbón aquifer but located in a non-active level. The cave comprises  
145 horizontal galleries and small rooms connected by shafts formed by phreatic circulation. Some rooms are  
146 well-decorated by large speleothems. The limestone thickness over the gallery where the stalagmite was  
147 collected is approximately 800 m.

### 148 **2.3. Cave climate**

149 Understanding the modern microclimatic and hydrological conditions of caves is import for a sound  
150 interpretation of speleothem proxy data (Genty et al., 2014; Lachniet, 2009; Moreno et al., 2014).  
151 Particularly, the transfer of the stable isotopic signal from the rainfall to the dripwater and, eventually, to  
152 the studied stalagmite is influenced by different processes in the atmosphere, soil and epikarst. Our  
153 preliminary results for the Pyrenees show a seasonal pattern of precipitation isotopes consistent with the  
154 annual temperature cycle (Moreno et al., 2021b). These data also suggest an interannual temperature– $\delta^{18}\text{O}$   
155 relationship of 0.47‰/°C (Giménez et al., 2021) that is only partially compensated by the -0.18 ‰/°C due  
156 to the water-calcite isotope fractionation (Tremaine et al., 2011) thus allowing to use  $\delta^{18}\text{O}$  in speleothems  
157 as a temperature indicator in this region (see also Bartolomé et al., 2015a; Bernal-Wormull et al., 2021).

158 From the four studied caves, the best monitored one is Seso cave where a detailed monitoring survey was  
159 conducted including analyses of  $\delta^{18}\text{O}$  variability in rainfall, soil water, dripwater and farmed calcite  
160 (Bartolomé, 2016). Seso cave developed under just few metres of rock, while the other caves are much  
161 deeper, allowing a faster response to rainfall variability in Seso dripwaters and speleothems. Monitoring  
162 carried out in Seso cave indicates a relationship between temperature and  $\delta^{18}\text{O}$  of rainfall observed at  
163 seasonal scale while rainfall isotopic composition is slightly modulated by the amount of precipitation  
164 (Bartolomé et al., 2015a).

## 165 **3. Methods**

### 166 **3.1. Speleothem samples**

167 This study is based on eight stalagmites from four different caves in Central Pyrenees (Fig. 1c, Table 1).  
168 The specimens were cut parallel to the growth axis and the central segment was sampled for U-Th dating,  
169 stable isotopes ( $\delta^{18}\text{O}$  and  $\delta^{13}\text{C}$ ) and Mg/Ca. Furthermore, the  $^{14}\text{C}$ -activity of multiple samples from the top  
170 of stalagmites MIC and XEV (both from Seso cave and underneath active drips) was determined in order  
171 to detect the atmospheric bomb peak induced by the nuclear tests in 1945-1963.

172 Four small stalagmites were obtained from Seso cave, all showing fine laminations consisting of pairs of  
173 dark-compact and light-porous laminae, but difficult to count due to their irregular pattern. The four Seso  
174 stalagmites show medium to high porosity in some intervals, usually more frequent towards the top. MIC  
175 (8.5 cm long) and XEV (26 cm long, composed of two stacked stalagmites – Appendix Fig. A1.a) were  
176 sampled from base to top. In stalagmites CHA (8.5 cm long) and in CLA (10.5 cm long), the uppermost  
177 interval was discarded due to the poor chronological control and associated to a possible hiatus above a  
178 macroscopic discontinuity (Fig. A1.a).

179 Stalagmites ISA (13.5 cm long, with a visual hiatus at 7 cm above the base) and LUC (23.3 cm long, also  
180 with a hiatus at 12.5 cm above the base) were sampled in Las Gloces cave (Fig. A1.b). Both are candle-  
181 shaped with a slight tilt in the growth axis above their respective hiatus. One stalagmite, TAR, was obtained  
182 from B1 cave which is an overgrowth over an older stalagmite composed of 7.5 cm of white carbonate that  
183 is slightly laminated towards the top (Fig. A1.c). Finally, a 80 cm-long stalagmite (JAR) was obtained from  
184 Pot au Feu cave. It is candle-shaped, laminated and lacks macroscopic hiatuses (Fig. A1.d).

### 185 **3.2. Stable isotope and Mg/Ca analyses**

186 Samples for stable isotopic ( $\delta^{18}\text{O}$  and  $\delta^{13}\text{C}$ ) analyses were microdrilled at 1-mm resolution along the growth  
187 axis of seven of the eight speleothems (JAR from Pot au Feu was sampled every 5 mm) using a 0.5 mm  
188 tungsten carbide dental bur. The first batch of the isotopic analyses was analysed at the University of  
189 Barcelona (Scientific-Technical Services), Spain, using a Finnigan-MAT 252 mass spectrometer, linked to  
190 a Kiel Carbonate Device III, with a reproducibility of 0.02‰ for  $\delta^{13}\text{C}$  and 0.06‰ for  $\delta^{18}\text{O}$ . Calibration to  
191 Vienna Pee Dee Belemnite (VPDB) was carried out by means of the NBS-19 standard. A second batch was  
192 analysed at the University of Innsbruck using a ThermoFisher Delta V Plus isotope ratio mass spectrometer  
193 coupled to a ThermoFisher GasBench II. Calibration of the instrument was accomplished using  
194 international reference materials and the results are also reported relative to VPDB. Long-term precision  
195 on the 1-sigma level is 0.06‰ and 0.08‰ for  $\delta^{13}\text{C}$  and  $\delta^{18}\text{O}$ , respectively (Spötl, 2011).

196 The elemental chemical composition was analysed in the eight stalagmites (every 1 mm in Las Gloces,  
197 Seso and B1 stalagmites and every 5 mm in JAR from Pot au Feu cave) using matrix-matched standards on  
198 an inductively coupled plasma-atomic emission spectrometer (Thermo ICAP DUO 6300 at the Pyrenean  
199 Institute of Ecology) following the procedure described in Moreno et al. (2010). Reported ratios are from  
200 measurement of Ca (315.8 nm) and Mg (279.5 nm), all in radial mode.

### 201 3.3. U-Th dating and $^{14}\text{C}$ bomb peak

202 A total of 55 samples were prepared for U-Th dating, according to the U and Th chemical procedures  
203 described in Edwards et al. (1987). Sample portions characterized by high porosity and voids were avoided  
204 to minimize the effect of open system behaviour and possible age inversions. From those 55 samples, 45  
205 were measured at the University of Minnesota (USA) and at the Xian' Jiaotong University (China) while  
206 10 samples were analysed at the University of Melbourne (Australia) (samples of JAR) using the  
207 methodology described in Hellstrom (2006). In the three laboratories, measurements were performed using  
208 a MC-ICP-MS (Thermo-Finnigan Neptune or Nu Instruments) following previously described methods  
209 (Cheng et al., 2013).

210 Due to the low U content (Table 2), the U-Th ages are not precise enough to obtain an accurate chronology  
211 for the recent speleothem growth (see large errors in top samples in Fig. A1). Therefore, the  $^{14}\text{C}$  “bomb  
212 peak” method was applied to the MIC and XEV stalagmites that were actively growing in Seso cave at the  
213 time of collection (2010 and 2013, respectively), confirmed by U/Th ages, albeit of low precision. We  
214 drilled 10 and 8 subsamples for MIC and XEV, respectively (Fig. 2a and b), and  $^{14}\text{C}$  activities were  
215 measured using a novel online sampling and analysis method combining laser ablation with accelerator  
216 mass spectrometry (LA-AMS) at the ETH Zurich (Welte et al., 2016). LA-AMS allows to produce spatially  
217 resolved  $^{14}\text{C}$  profiles of carbonate minerals with a precision of 1% for modern samples. The background  
218 measured on  $^{14}\text{C}$ -free marble ( $F^{14}\text{C} = 0.011 \pm 0.002$ ) is low and reference carbonate material is well  
219 reproduced. This method relies on the exploitation of the global anthropogenic increase in atmospheric  $^{14}\text{C}$   
220 resulting from nuclear testing predominately in the 1950s and 1960s CE as a chronological marker in the  
221 mid to late 20<sup>th</sup> Century (e.g., Genty et al., 1998; Hua et al., 2012). Atmospheric  $^{14}\text{C}$  concentrations began  
222 to rise in 1955 CE, peaking in the Northern Hemisphere (NH) in 1963 CE (Reimer, 2004). Because 80 to  
223 90% of the carbon found in most speleothems comes from soil  $\text{CO}_2$ , this being linked to atmosphere  $\text{CO}_2$ ,  
224 it is likely that speleothem  $^{14}\text{C}$  activity is close to the atmospheric  $^{14}\text{C}$  activity or at least to the soil activity  
225 (Markowska et al., 2019). Thus, the point where the  $^{14}\text{C}$  concentration begins to rise, the highest  
226 concentration point, and the date when the speleothem was removed from the cave (if actively dripping)  
227 were used as chronological anchor points (Fig. 2a and b).

### 228 3.4. Age model

229 Age models were produced using StalAge software (Scholz and Hoffmann, 2011) for the eight speleothems  
230 (Fig. A1) using the U-Th dates presented in Table 2. In the ISA stalagmite, one date was discarded due to  
231 the large error (indicated in red in Table 2). During several intervals, two or more stalagmites grew  
232 contemporaneously, allowing to test the reproducibility of the proxy records. We made the a priori  
233 assumption that the  $\delta^{18}\text{O}$  data of the selected stalagmites record a common rainfall and temperature signal,

234 given that these caves were only 20 km apart (Fig.1c). Then, the records are combined with *Iscam*  
235 (Fohlmeister, 2012), a method that correlates dated proxy signals from several stalagmites, determines the  
236 most probable age-depth model, and calculates the age uncertainty for the combined record.

237 In order to minimize the effect of different absolute isotopic values and ranges of individual stalagmite data  
238 series, we detrended and normalized the  $\delta^{18}\text{O}$  series using *Iscam*. Doing so, the interpretation of absolute  
239 values will be precluded. Regarding the other parameters that can be changed in *Iscam*, we used point-wise  
240 linear interpolation, 1000 Monte Carlo simulations and the smoothing window was fixed at 10 years. The  
241 stalagmites were included in the *Iscam* composite record from the oldest to the youngest one as was the  
242 order that provided the highest correlation coefficients: JAR- LUC – ISA -TAR – CHA – CLA -XEV and  
243 MIC. The ISA sample was treated as two parts (ISA top and ISA base) to account for the hiatus, while LUC  
244 was regarded as only one as *StalAge* does not suggest a hiatus in this stalagmite (Fig. A1.b). For the two  
245 stalagmites that were active when collected, MIC and XEV, we also produced a composite record for the  
246 last 200 years using *Iscam* (Fig. 2c). The use of *Iscam* software minimized the age uncertainty being lower  
247 than the error in the U-Th dates. As an example, for last 600 years, the uncertainty is below 20 years.  
248 However, it may reach 100 years for some particular intervals (eg. the century 1350-1250 AD).

249 In order to explore correlations among stalagmites from the same caves, we repeated the procedure to obtain  
250 a composite record for the four stalagmites from Seso cave (CHA, CLA, XEV and MIC) (Fig. A2) and the  
251 two from Las Gloces cave (ISA and LUC) (Fig. A3). In those two cases, we did not detrend or normalize  
252 the individual records since they belong to the same cave and show the same range of  $\delta^{18}\text{O}$  values. These  
253 four records (composite records from Las Gloces and Seso caves, and individual stalagmites from Pot au  
254 Feu and B1 caves) are show in Fig. 3 and compared to the final composite record. The composite  $\delta^{18}\text{O}$   
255 record is used in this article as a proxy record for the Central Pyrenees climate of last 2500 years. We have  
256 used approximate onset and end of five time subperiods, following previous literature (eg. Sánchez-López  
257 et al., 2016): the end of the RP at 450 CE; DA (450-850 CE), MCA (850-1250 CE), LIA (1250-1950 CE)  
258 and IE (since 1850 CE).

### 259 **3.5. Statistical analyses**

260 Statistical analyses were carried out using PAST software (Hammer et al., 2001). The  $\delta^{18}\text{O}$  series and the  
261 instrumental climatic series were first resampled (linear interpolation) to obtain the same regular spacing  
262 (annual). Then, correlation was computed using Spearman's rank correlation analysis, a nonparametric  
263 measure as an alternative to Pearson correlation analysis. This analysis was preferred to account for  
264 nonlinear relationships, with  $r$  indicating the correlation coefficient and  $p$ -value, the probability value of  
265 that correlation. The Bonferroni test was applied to prevent data from spuriously appearing as statistically  
266 significant by making an adjustment during comparison testing (PAST software; Hammer et al, 2001).

267

## 268 **4. Results**

### 269 **4.1. Age models and composite record**

#### 270 **4.1.1. Detection of the bomb peak and composite record of the last 200 years**

271 Stalagmites MIC and XEV from Seso cave were actively dripping when removed from the cave (in 2010  
272 and 2013, respectively). Calcite deposited on glass plates placed below the two dripping points and  
273 collected seasonally until 2021 demonstrates that the drip water is supersaturated with respect to calcite and  
274 suggests that the top layer of both stalagmites was formed during the respective collection year (Fig. 2).  
275 Therefore, these two stalagmites were analysed for their  $^{14}\text{C}$  activity to identify the “bomb peak” and  
276 improve the age model.

277 A strong increase in the  $^{14}\text{C}$  activity is registered in the MIC and XEV stalagmites at 16 mm and 40 mm  
278 depth from top (dft), respectively (Fig. 2a and b) with a rise in the fraction modern  $F^{14}\text{C}$ , interpreted as the

279 start of the mid-20<sup>th</sup> century atmospheric bomb peak. This allows defining the year 1955 CE, within  $\pm 2$ yr  
280 uncertainties, at 16 mm dft in MIC and 40 mm dft in XEV (Fig. 2). All radiocarbon bomb peaks published  
281 from speleothems show that the response of speleothem <sup>14</sup>C activity to the increase in atmospheric  
282 radiocarbon activity occurred nearly simultaneously. However, whether the <sup>14</sup>C activity peak in a  
283 speleothem can be assigned to the year 1963 CE depends on the soil properties and the thickness of the  
284 rock above the cave, as well as the delay in the transfer of the atmospheric <sup>14</sup>C signal to the speleothem  
285 (Fohlmeister et al., 2011; Hua et al., 2017). In the case of Seso cave, which is just 2-3 m below the surface  
286 and the soils are patchy and thin (Bartolomé, 2016), the transfer of the <sup>14</sup>C signal was likely fast. We  
287 therefore place the year 1963 CE, within  $\pm 2$ yr uncertainties, at 11 mm dft in MIC and at 25 mm dft in XEV  
288 (Fig. 2a and b).

289 Since the two stalagmites MIC and XEV are the only ones in this study whose records extend to modern  
290 times, we compare them with the instrumental record in order to improve the interpretation of the stable  
291 isotope data. Thus, MIC and XEV  $\delta^{18}\text{O}$  data were first combined using *Iscam* (Fig. 2c). Using the  
292 parameters indicated in Methods (section 3.3), but without normalizing the records (both stalagmites belong  
293 to the same cave and show the same range of  $\delta^{18}\text{O}$  values) the correlation of stalagmites MIC and XEV  
294 provided by *Iscam* software ( $r$  is 0.81 (95% significance). This composite  $\delta^{18}\text{O}$  record covers the last 200  
295 years and has an amplitude of 0.9 ‰. The main feature (Fig. 2c) is a trend towards less negative values  
296 (indicated by a polynomial line in Fig. 2c).

#### 297 **4.1.2. StalAge models and *Iscam* stack**

298 Age models obtained by StalAge for individual stalagmites indicate that the growth rate was quite stable,  
299 except of ISA and LUC, both from Las Gloces cave, where the growth rate changed after hiatuses (Fig.  
300 A1.B). The temporal resolution of the stable isotope data allows to explore changes occurring on a decadal  
301 scale (Table 1).

302 Using the parameters for constructing a composite record using *Iscam* (see Methods), correlation ( $r$ ) value  
303 (95% significance) of stalagmite JAR and LUC is 0.48, 0.67 between ISA\_base and the combined stack of  
304 JAR-LUC, 0.65 between ISA\_top and the previous stack, 0.74 between TAR and the previous stack, 0.79  
305 between CHA and the previous stack, 0.95 between CLA and the previous stack, 0.71 between XEV and  
306 the previous stack and finally, 0.53 between MIC and the previous stack. These values demonstrate a  
307 statistically significant correlation among the individual stalagmites and a higher correlation than between  
308 the original time series. The composite  $\delta^{18}\text{O}$  record was compared to the composite records from Seso (Fig.  
309 A3) and Las Gloces (Fig. A4) caves and the two individual stalagmites from the other two caves (Fig. 3).  
310 This comparison shows that many of the main features of the original records are also well recorded in the  
311 composite (Fig. 3). One example is the interval 530-550 CE during the Dark Ages characterized by  
312 relatively low  $\delta^{18}\text{O}$  values in Las Gloces and Pot au Feu cave records (black arrows in Fig. 3), or the interval  
313 at the end of the LIA (1675-1750 CE) with less negative  $\delta^{18}\text{O}$  values in Seso, B1 and Las Gloces cave  
314 records (this interval is recorded in five stalagmites: CHA, XEV, TAR, LUC and ISA, Figs. A1).

#### 315 **4.2. Individual isotopic and Mg/Ca profiles and composite $\delta^{18}\text{O}$ record**

316 The isotopic ( $\delta^{18}\text{O}$  and  $\delta^{13}\text{C}$ ) and Mg/Ca profiles are shown for the eight stalagmites, using their StalAge  
317 models (Fig. A1) for the four caves studied (Seso, Las Gloces, B1 and Pot au Feu). In general,  $\delta^{18}\text{O}$  and  
318  $\delta^{13}\text{C}$  are not well correlated ( $r \sim -0.3-0.4$ ;  $p$ -values indicating no significant correlation) with the exception  
319 of TAR ( $r > 0.8$ ) and CHA ( $r = 0.5$ ). Generally,  $\delta^{13}\text{C}$  is better correlated with Mg/Ca pointing to a  
320 hydrological link of these proxies, via changes in prior calcite precipitation (PCP) associated with the longer  
321 residence time of the water in the soil and epikarst during dry periods (Genty et al., 2006; Moreno et al.,  
322 2010). A similar interpretation was suggested for other Holocene records from northeastern Spanish caves,  
323 such as speleothems from Molinos-Ejulve caves in the Iberian Range (Moreno et al., 2017) and records  
324 covering the last deglaciation in the Pyrenees (Bartolomé et al., 2015a). However,  $\delta^{13}\text{C}$  and Mg/Ca are  
325 highly variable in absolute values and patterns among caves, and further studies are required to better  
326 constrain the climate-proxy transfer functions for two parameters. Therefore, we base our paleoclimate

327 interpretations on the oxygen isotopes which are known to show a more robust response to regional climate  
328 change.

329 The composite  $\delta^{18}\text{O}$  record for the Central Pyrenees of the last 2500 years is shown in Fig. 3. The highest  
330  $\delta^{18}\text{O}$  values of last 2500 years were reached during the RP (50 BCE-250 CE). The MCA is characterized  
331 by two intervals of relatively high values (900-950 CE and 1150-1250 CE) and also the LIA shows a one  
332 such interval (1675-1750 CE). In contrast, the Dark Ages are characterised by consistently low values. In  
333 fact, the most negative interval of last 2500 years is reached at ~520 CE, a well-known cold episode related  
334 to volcanic eruptions (see section 5.2). A long interval with low  $\delta^{18}\text{O}$  values corresponds to the onset of the  
335 LIA (1250-1500 CE, with two very negative excursions) as well as the end of the LIA (1750-1850 CE).  
336 The most remarkable feature of the MCA and LIA is the large centennial-scale variability. In fact, the LIA  
337 has a clear tripartite pattern, with two intervals of low values at the onset and end and less negative values  
338 in between. In contrast, the MCA pattern, although also tripartite, it is characterized by two intervals of less  
339 negative values at the onset and end, and a short period of low values in between. An interval with high  
340  $\delta^{18}\text{O}$  values is observed since 1950 CE (Fig. 3).

341

## 342 **5. Discussion**

### 343 **5.1. Interpretation of $\delta^{18}\text{O}$ data**

344 Under equilibrium conditions, the  $\delta^{18}\text{O}$  value of speleothem carbonate is related to just two variables: the  
345  $\delta^{18}\text{O}$  value of the drip water, and the cave temperature through its control on equilibrium isotope  
346 fractionation between water and calcite (Lachniet, 2009). Over the CE, air temperature in a given cave  
347 likely changed very little ( $< 1\text{ }^\circ\text{C}$  corresponding to  $\sim 0.18\text{‰}$  in stalagmite  $\delta^{18}\text{O}$ , following Tremaine et al.,  
348 2011) (PAGES Hydro2k Consortium, 2017) such that the observed  $\delta^{18}\text{O}$  variations in these Pyrenean  
349 speleothems of more than  $1\text{‰}$  are governed primarily by the  $\delta^{18}\text{O}$  variability of the drip water.

350 For a constant sea-surface  $\delta^{18}\text{O}_{\text{sw}}$  value, as it is expected for this time period, event-scale monitoring of the  
351 isotopic composition of oxygen in the rainwater ( $\delta^{18}\text{O}_r$ ) in different areas of the Iberian Peninsula constrains  
352 some of the drivers of rainfall isotopic fractionation (Moreno et al., 2021b). Recent rainfall monitoring  
353 surveys in the Central Pyrenees indicate that the values of  $\delta^{18}\text{O}_r$  show an interannual dependence on  
354 temperature equivalent to  $0.47\text{--}0.52\text{‰}/^\circ\text{C}$ , depending on the site (Giménez et al., 2021; Moreno et al.,  
355 2021a). This dependence is only partially offset by the empirical value of isotope fractionation during  
356 calcite precipitation ( $-0.18\text{‰}/^\circ\text{C}$ ; Tremaine et al., 2011) thus allowing to consider temperature as one  
357 important factor driving  $\delta^{18}\text{O}$  variability. Apparently, the rainfall amount does not strongly control the  
358 isotopic values at event-scale, but analysing the  $\delta^{18}\text{O}_r$  variation through time, added to the strong  
359 dependence on air temperature, it is clearly observed how the most intense rainfall events together with the  
360 longest lasting rain events (several days) resulted in an isotopic lightening (Giménez et al., 2021). Thus, we  
361 consider that dripwater  $\delta^{18}\text{O}_{\text{dw}}$  is driving the  $\delta^{18}\text{O}_c$  signal in the stalagmites and, very likely, air temperature  
362 and precipitation amount will be modulating its variability along last 2500 years.

363 The  $\delta^{18}\text{O}$  composite record, based on the combination of MIC and XEV  $\delta^{18}\text{O}$  data, provides the opportunity  
364 to correlate with instrumental temperature and precipitation amount data (Fig. A4 and A5). It is worth to  
365 note that the chronological control of  $\delta^{18}\text{O}$  data is robust at decadal-scale, thus limiting an annual accurate  
366 correlation. In spite temperature records in the region of the studied caves are, unfortunately, scarce and  
367 short (e.g., the Goriz hut station covers only the last 50 years, Fig. A4b) there are two exceptions. First, the  
368 homogenized MAAT dataset since 1882 from the Pic du Midi de Bigorre meteorological station (2860 m  
369 a.s.l. in the French Pyrenees) (Bücher and Dessens, 1991; Dessens and Bücher, 1995), which started in  
370 1882 CE, is the currently longest one from the Pyrenees (Fig. A4c). And, second, the temperature and  
371 precipitation reconstruction by Pérez-Zanón et al. (2017) based on 155 stations from the Central Pyrenees  
372 starting in 1910 CE (Fig. A4d). Comparing the MIC and XEV  $\delta^{18}\text{O}$  data with those temperature datasets a  
373 significant correlation is found with Pic du Midi de Bigorre mean annual minima temperature ( $\sigma_s = 0.32$ ; p-  
374 value  $< 0.005$ ). Likely, the other temperature records were too short to generate a significant correlation.



375 Additionally, when comparing our  $\delta^{18}\text{O}$  stack with the HadCRU5 reconstruction for the mean Northern  
376 Hemisphere temperatures (Morice et al., 2021) (Fig. A4e), the correlation is higher and significant ( $\sigma_s$   
377  $=0.49$ ;  $p\text{-value}<0.005$ ). We suspect that the length of this last series (150 years) together with a large spatial  
378 scale leads to a better correlation with the speleothem composite. However, a large part of the variance  
379 remains to be explained by other factors (i.e. precipitation changes in source, seasonality or amount). Using  
380 these relationships as a guide and considering all the isotopic change related to temperature change, the  
381 observed variation of  $0.30 - 0.32 \text{ ‰}$  in  $\delta^{18}\text{O}$  of our composite would represent a change of  $1^\circ\text{C}$  (Fig. A4),  
382 that appears quite plausible for the studied period.

383 The influence of precipitation amount variability on the isotopic composition of speleothem composite is  
384 evident from 1970 to 1980 CE, a relatively cool interval in the Pyrenees but characterized by a sustained  
385 decrease in the amount of precipitation (Pérez-Zanón et al., 2017) (Fig. A5, note reversed axis for  
386 precipitation). For this interval, the relationship between the  $\delta^{18}\text{O}$  composite and temperature series is  
387 reversed, as the low precipitation leads to higher  $\delta^{18}\text{O}$  values (as if they represented higher air temperatures).  
388 On the contrary, a rapid increase in precipitation at ca. 1960 without any important change in temperature,  
389 results in a negative peak on the  $\delta^{18}\text{O}$  speleothem composite (Fig. A5). This shows that, in spite air  
390 temperature being an important factor influencing  $\delta^{18}\text{O}$  variability in speleothems from the Pyrenees, other  
391 processes such as the amount of precipitation, its seasonality distribution or even its source(s) may be also  
392 a significant controlling factor (Priestley et al., 2023; Treble et al., 2022), especially when extreme values  
393 are reached (very dry or very wet time intervals), as was indicated by rainfall studies in the Pyrenees  
394 (Giménez et al., 2021; Moreno et al., 2021a). In any case, MIC and XEV  $\delta^{18}\text{O}$  data are not significantly  
395 correlated with any of the precipitation data from Fig. A5.

396 Finally, it is important to note that the  $\delta^{18}\text{O}$  values in the different caves varied at distinct range (Fig. 3).  
397 Thus, when producing the composite record, the  $\delta^{18}\text{O}$  profiles of the eight stalagmites were normalized and  
398 detrended with the aim of combining different caves. With such a procedure, comparing relative  
399 temperature changes coming from different time periods is not possible. Thus, for example, comparing the  
400 warming magnitude of the RP with the MCA or with the IE is not feasible since data were obtained from  
401 different caves and were previously normalized and detrended. Unfortunately, none of our stalagmites  
402 cover continuously from a warm period, i.e. the MCA, to current conditions to compare values. Therefore,  
403 the ability of current data to accurately quantify changes in temperature for last 2500 years in the Central  
404 Pyrenees is limited. Normalized  $\delta^{18}\text{O}$  composite record is evaluated in the context of previous local,  
405 regional and global information.

## 406 **5.2 Climate reconstruction for the last 2500 years**

407 The Pyrenees is a region threatened by global warming, where the impact on biodiversity, elements of the  
408 mountain cryosphere such as glaciers or ice caves, and water resources has been increasing in recent  
409 decades (<https://www.opcc-ctp.org>). The  $\delta^{18}\text{O}$  composite constructed using eight speleothems represents  
410 the first climate reconstruction based on speleothems for this region covering the last 2500 years and  
411 provides an excellent opportunity to reconstruct natural variability and disentangle main driving  
412 mechanisms. We compare it first with other climate series from the Pyrenees and northern Iberia (section  
413 5.2.1) and, then, with available speleothems from Europe and western Mediterranean to obtain a regional  
414 overview (section 5.2.2). Finally, a short discussion about the potential drivers of main observed changes  
415 is provided (section 5.2.3).

### 416 **5.2.1. The last 2500 years in the context of the Iberian Peninsula**

417 Previous climate reconstructions for the CE from the Pyrenees were mostly based on lake records (e.g.,  
418 González-Sampériz et al., 2017), tree-ring data (e.g., Büntgen et al., 2017), and few data from glaciers or  
419 ice caves (Moreno et al., 2021b; Oliva et al., 2018; Sancho et al., 2018; Leunda et al., 2019). Despite large  
420 variability, these records reveal a clear distinction between relatively cold (DA, LIA) and warm (RP, MCA)

421 periods, which were generally characterized by high and low lake levels, respectively. The differences and  
422 similarities among Pyrenean records merit a more detailed evaluation, organized by chronological periods.

423 A. The Iberian - Roman period in the Pyrenees. Considering the last 2500 years, the RP stands out as a  
424 clear warm period from the speleothem composite record (Fig. 4a). In the Eastern Pyrenees, Redon Lake  
425 records low winter-spring temperatures with a warming trend at the end (Pla and Catalan, 2005; Pla-Rabes  
426 and Catalan, 2011), whereas the summer-autumn temperatures show a transition from cold to warm  
427 (Catalan et al., 2009). Not many high-resolution Pyrenean lake records exist for this period (e.g. Corella et  
428 al., 2016; Vegas-Vilarrúbia et al., 2022) and dendrochronological studies in this mountain range do not  
429 cover this time period. Thus, an interesting record to compare with is the A294 ice cave in the Cotiella  
430 massif (Sancho et al., 2018). This 9-m thick ice is divided into intervals of low and high snow accumulation,  
431 requiring moist and cold conditions to form. The fourth (and last) stage of this ice deposit indicates a high  
432 accumulation rate (Fig. 4d), thus a relatively humid and cold period, from 500 BC to 62 CE. Afterwards,  
433 the record stopped reflecting the onset of a warmer and drier climate (Sancho et al., 2018) associated with  
434 the RP thermal maximum (Fig 4a). Recently, not yet published observations indicate the ice deposit grew  
435 during the cold/wet years associated to the DA (M. Bartolomé, personal communication). In our speleothem  
436 composite, the RP is represented by Las Gloces and Pot au Feu stalagmites that show less negative values  
437 (Fig. 3), which suggest rather warm, and probably dry conditions in the Central Pyrenees during the RP,  
438 particularly between 0 to 200 CE (Fig. 4). This is supported by data showing retreating glaciers in the  
439 Pyrenees at that time (Moreno et al., 2021b).

440 B. The Dark Ages in the Pyrenees. This period is characterized in our speleothem composite by cold-wet  
441 climates starting ca. 300 CE, with two particular cold events at 500-650 CE and 750-850 CE and a warmer-  
442 drier interval in between (650-750 CE) (Fig. 4a). Pyrenean lake records also point to cold and wet conditions  
443 but with a high heterogeneity and low resolution, thus preventing a detailed characterization of this time  
444 period (González-Sampériz et al., 2017). For example, Estanya Lake recorded a dominant dry climate  
445 between 500 and 750 CE (Fig. 4c), changing to higher lake levels afterwards (Morellón et al., 2009), a  
446 pattern that is quite coherent with the speleothem composite. Proxy data from Redon Lake suggest cold  
447 winter-spring temperatures in the Eastern Pyrenees during the DA (Pla and Catalan, 2005, 2011).

448 C. The Medieval Climate Anomaly in the Pyrenees. The large centennial-scale temperature variability  
449 recorded by the speleothem composite is particularly well expressed for the MCA and the LIA, with three  
450 distinct intervals of temperature changes (yellow and blue bands in Fig. 4a), thus revealing a more complex  
451 pattern as previously inferred by lower resolution records (e.g., Moreno et al., 2012; Sánchez-López et al.,  
452 2016). The MCA has been interpreted as a “warm and dry” climate regime in the Southern Pyrenees  
453 (Morellón et al., 2012) (Fig. 4c), characterized by low lake levels and more abundant xerophytic vegetation.  
454 Our new data show, however, that a colder (maybe wetter) interval between 950 and 1050 CE separated  
455 two clear warm periods before (900-950 CE) and after (1150-1250 CE; Fig. 3). This cold interval was also  
456 identified in the Redon Lake record as a sudden cooling about 1000 years ago (Pla and Catalan, 2005).  
457 Interestingly, this cold century was not observed by an increase in heavy precipitation in the Montcortés  
458 lake record (Fig. 4b).

459 D. The Little Ice Age in the Pyrenees. The LIA climate variability is well-characterized in the Pyrenees  
460 thanks to records from glaciers, such as moraines associated with glacier advances, but also due to historical  
461 documents such as pictures or old photographs (Oliva et al., 2018). The available information indicates that  
462 the LIA glaciers in the Pyrenees occupied 3366 ha in 1876, just 810 ha in 1984 and these glaciers have lost  
463 23.2% of their volume considering only from 2011 to 2020 (Hughes, 2018; Vidaller et al., 2021). In many  
464 Pyrenean valleys, more than one moraine belt was assigned to the LIA (García-Ruiz et al., 2014) but,  
465 unfortunately, the discontinuous character of these landforms and difficulties in dating them does not allow  
466 to resolve the internal pattern of the LIA in the Pyrenees. A recent compilation of records across the Iberian  
467 mountains proposed several climate phases during the LIA (Oliva et al., 2018), which are well-correlated  
468 with our speleothem composite (Fig. 4a): A first cooling phase lasted from the onset of the LIA (ca. 1200  
469 CE) until 1480 CE, followed by relatively warmer conditions from 1480 to 1570 CE. A second phase of  
470 gradual cooling occurred until 1600 CE followed by very cool conditions lasting until 1715 CE and

471 coinciding with the Maunder Minimum (1645 – 1715CE). In our speleothem composite, this interval is  
472 well defined as a cold period but it was not the one with minimum  $\delta^{18}\text{O}$  values of the LIA (Fig. 4a). The  
473 first half of the 18<sup>th</sup> century was characterized by warm conditions, supported by many records compiled  
474 by Oliva et al. (2018). After 1760 and until the end of the LIA (ca. 1850 CE), a climate deterioration and  
475 more frequent extreme climate events were described. This last cold phase is also captured by the  
476 speleothem composite and may correspond to the Dalton Minimum (1790 – 1830 CE). It is characterised  
477 by large climate variability and lasted until about 1850 CE.

478 E. The Industrial Era in the Pyrenees. The Industrial Era (IE), defined as the last 150 years, is characterized  
479 in the Pyrenean speleothem composite by low temperatures that started to increase at about 1950 CE (Fig.  
480 4a), in response to the Great Acceleration (Steffen et al., 2015) (yellow band in Fig.4). This increase of  
481 temperature is well recorded in other Pyrenean climate archives, such as glaciers or lake records. Thus, the  
482 last 150 years were marked by a gradual glacier retreat since 1850 CE that accelerated specially after 1980  
483 CE, considered as a “tipping point” in glacier retreat not only on a Pyrenean scale (López-Moreno et al.,  
484 2016) but also on a global scale (Beniston et al., 2018). A decrease in heavy rainfall (Fig. 4b) and an increase  
485 in salinity (Fig. 4c) are well defined in Montcortés and Estanya lake records, respectively, during the IE,  
486 indicating a decrease in the amount of precipitation in a, likely, drier scenario. Besides these two lake  
487 records, high-altitude lakes show a significant increase in primary productivity during the last decades  
488 (Vicente de Vera García et al., 2023). These recent results demonstrate the combined impacts of climate  
489 change and increased human pressure in the Pyrenees. Coherently, last 50 years are characterized by  
490 generally enriched  $\delta^{18}\text{O}$  values in our speleothem record (yellow bands in Fig. 4). However, the last two  
491 decades (our record ends in 2013, the year XEV sample was collected) are not the ones with the highest  
492  $\delta^{18}\text{O}$  values (Fig. 4a) as also observed in tree-ring data from the Spanish Central Pyrenees (Büntgen et al.,  
493 2017) (Fig. 4e). One potential explanation for the lack of exceptionally high  $\delta^{18}\text{O}$  values would be a slight  
494 increase in precipitation amount. Thus, precipitation reconstruction for the Pyrenees during the last two  
495 decades indicate slightly higher values than those of previous decades (Pérez-Zanón et al., 2017, Fig. A.5).  
496 Other factors, such as changes in the precipitation source or type (eg. dominance of Atlantic frontal rainfall  
497 versus Mediterranean convective episodes) may be also behind the recorded  $\delta^{18}\text{O}$  values of last decades.

## 498 **5.2.2. Temperature variability in W Europe and the W Mediterranean during last 2500 years**

499 The PAGES2k European temperature record is the most recent compilation of the last two millennia at  
500 European scale (PAGES 2k Consortium, 2013) and it is coherent with our speleothem composite for the  
501 Central Pyrenees (Fig. 6). This comparison shows a synchronicity for several of the warmest intervals of  
502 the CE, such as the first centuries CE in the RP, the 1150-1250 CE period within the MCA, and the last  
503 decades (marked as orange bars in Fig. 6). There are very few high-resolution speleothem records in Europe  
504 covering the CE (Comas-Bru et al., 2020); we selected nine speleothems records in Europe and northern  
505 Africa which cover with robust chronology and decadal resolution the last 2500 years (Fig. 5). One of these  
506 records is interpreted as NAO variability (Baker et al., 2015), three are paleo-precipitation reconstructions  
507 (Ait Brahim et al., 2019; Cisneros et al., 2021; Thatcher et al., 2022) and the other five are reflecting paleo-  
508 temperature variations (Affolter et al., 2019; Fohlmeister et al., 2012; Mangini et al., 2005; Martín-Chivelet  
509 et al., 2011; Sundqvist et al., 2010). Considering these differences in the interpretation and the fact these  
510 records are from different regions with different climates (from Sweden to Morocco), dissimilar profiles of  
511 paleoclimate variability can be expected. Still, some features are comparable and can be discussed to obtain  
512 a super-regional picture.

513 A. The Roman period in Europe-W Mediterranean. In Europe, and particularly in the Mediterranean region,  
514 the RP is well-known as a warm period (e.g., McCormick et al., 2012). The average sea-surface temperature  
515 in the western Mediterranean Sea was 2°C higher than the average temperature of the late centuries  
516 (Margaritelli et al., 2020). Our composite, with high values of normalized  $\delta^{18}\text{O}$  values during the whole  
517 RP, and particularly from 0-200 CE, agrees with the scenario of warm temperatures (Fig. 5i). Speleothem  
518 data from the Balearic Islands (Cisneros et al., 2021) indicate a transition from humid to dry conditions  
519 along the Iberian-RP (Fig. 5c). The dry period at the end of the RP in the Balearic record, appears in

520 agreement with a new speleothem record from northern Italy (Hu et al., 2022), suggesting that the observed  
521 drying trend was a possible contribution to the collapse of the Roman Empire in 476 CE. Record from  
522 Morocco (Ait Brahim et al., 2019), contrarily, marks a humid trend at the end of the RP (Fig. 5d). Similarly,  
523 an increase in humidity was observed in southern Iberia during the RP (Jiménez-Moreno et al., 2013;  
524 Martín-Puertas et al., 2009) thus reflecting a large spatial heterogeneity in precipitation amount when  
525 comparing records from the north and south of the Mediterranean basin.

526 B. The Dark Ages in Europe-W Mediterranean. After the RP, the cold Dark Ages started (450-850 CE).  
527 Part of this period is known as the “Late Antique Little Ice Age” (LALIA), lasting from 536 CE to 670 CE,  
528 characterized by specially cold conditions in Europe (Büntgen et al., 2016). Our speleothem composite  
529 shows in general cold-wet conditions, but with centennial-scale variability during the DA (Fig. 5). Three  
530 clear intervals can be defined, following the  $\delta^{18}\text{O}$  pattern of our composite, as well as speleothem records  
531 from the Alps (Mangini et al., 2005) and Central Europe (Affolter et al., 2019; Fohlmeister et al., 2012): an  
532 initial cooling phase corresponding to the LALIA (ca. 500-650 CE), a warming phase (ca. 650-750 CE)  
533 and a final cooling phase right before the onset of the warming associated with the MCA (ca 750-850 CE).  
534 A  $\delta^{13}\text{C}$  speleothem record from three N Iberian caves (Martín-Chivelet et al., 2011) shows a warming trend  
535 in the DA period but with internal variability that, within dating uncertainties, can be related to the three  
536 phases defined above (Fig. 5i). It is worth noting that the period with the most negative  $\delta^{18}\text{O}$  values recorded  
537 in the speleothem composite from the Pyrenees corresponds to the LALIA decades, a cooling period which  
538 provoked widespread social disruption in Europe, famine, and episodes of epidemic diseases (Peregrine,  
539 2020).

540 C. The Medieval Climate Anomaly in Europe-W Mediterranean. The MCA was one of the warmest periods  
541 in continental Europe (and the W Mediterranean, Lüning et al., 2019) of the CE, usually dated to 900 CE  
542 to 1300 CE and characterized by warm (Goosse et al., 2012) and relatively dry conditions (Helama et al.,  
543 2009). The MCA was also characterized by a general glacier retreat, mainly associated with a decline in  
544 precipitation amount in the Alps (Holzhauser et al., 2016) and the Pyrenees (Moreno et al., 2021b). This  
545 scenario is supported by speleothem records from Europe and the W Mediterranean (Fig. 5), which all point  
546 to generally warm (Affolter et al., 2019; Fohlmeister et al., 2012; Mangini et al., 2005; Martín-Chivelet et  
547 al., 2011; Sundqvist et al., 2010) and/or dry conditions (Ait Brahim et al., 2019; Baker et al., 2015; Thatcher  
548 et al., 2022), even leading to speleothem growth stops as for example seen in the Balearic record (Cisneros  
549 et al., 2021). Previous studies have emphasized the complexity of the spatial and seasonal structure of the  
550 MCA in Europe (Goosse et al., 2012). The selected speleothem records underscore this complexity,  
551 particularly considering that in our Pyrenean composite one of the periods marked as cold-wet occurred  
552 during the MCA, ca. 950-1050 CE (Fig. 5). We propose that this cold interval represents the climate  
553 response to the Oort solar minimum in the Pyrenees, a time period characterized by low number of sunspots  
554 covering spanning 1010 to 1050 CE (Bard et al., 2000).

555 D. The Little Ice Age in Europe-W Mediterranean. The LIA is well known in Europe and the W  
556 Mediterranean region, characterized by cold temperatures and relatively humid conditions as recorded, for  
557 example, in chironomid-inferred summer temperatures (Ilyashuk et al., 2019), Mediterranean SSTs  
558 (Cisneros et al., 2016), the advance of alpine glaciers (Holzhauser et al., 2016) and the rise of lake levels  
559 (Magny, 2013). The LIA cooling, however, was not continuous and uniform in space and time. Regarding  
560 temperatures, many of the available reconstructions from the Alps (Trachsel et al., 2012), Scandinavia  
561 (Zawiska et al., 2017), and other regions of Europe (Luterbacher et al., 2016), provide evidence for a main  
562 LIA cooling phase which was divided into three parts: two cold intervals with a slightly warmer episode in  
563 between, with the most severe cooling during the 18<sup>th</sup> century (Ilyashuk et al., 2019). This pattern is also  
564 found in the two temperature records from Iberian speleothems (this study and the one from Martín-  
565 Chivelet et al., 2011) and a temperature record from the Alps (Mangini et al., 2005) (Fig. 5, marked by  
566 arrows). The other European speleothem records show only two phases during the LIA: a longer and intense  
567 cooling period followed by a warming (Fig. 5, Affolter et al., 2019; Fohlmeister et al., 2012; Sundqvist et  
568 al., 2010). A tripartite pattern is recorded by humidity-sensitive speleothems from Portugal, with wet-dry-  
569 wet conditions in excellent agreement with the cold-warm-cold pattern in the Pyrenean record (this study),

570 supporting the concept that this pattern is controlled by changes in intensity and N-S migration of the Azores  
571 High (Thatcher et al., 2022).

572 E. The Industrial Era in Europe-W Mediterranean. Between about 1870 CE and today, an increase in  
573 temperature is detected by European speleothem records (Fig. 5), as previously shown by the retreat of  
574 European glaciers (Beniston et al., 2018) and tree-ring summer temperature records (Büntgen et al., 2011)  
575 as well as drought reconstructions (Büntgen et al., 2021). The impacts in Europe and the W Mediterranean  
576 of the current global warming trend, accelerated during last 50 years, are becoming more and more evident  
577 (Jacob et al., 2018; Naumann et al., 2021).

### 578 **5.2.3 Drivers of past temperature variability in the Pyrenees**

579 The good correlation and synchronicity between the PAGES2k European record and the Pyrenean  
580 composite (marked as orange bars in Fig. 6) supports the interpretation of temperature being the dominant  
581 factor in controlling the speleothem record. This centennial-scale correlation can be extended to a  
582 worldwide tree-ring compilation (Sigl et al., 2015) pointing to the presence of common warm periods in  
583 the Central Pyrenees. Interestingly, if precipitation amount was the dominant factor controlling the  $\delta^{18}\text{O}$   
584 speleothem composite, it would be difficult to find a common signal at regional or even continental scale,  
585 as indicated by the overall good correlation shown in Fig. 6.

586 It is worth to mention the good correlation with several especially cold periods at decadal scale (blue bars  
587 in Fig. 6), such as the event at 540-550 CE (registered at 520 CE in the speleothem record) or two cold  
588 spikes at 800-850 CE at the end of the DA. We proposed that the cold event at ca. 540 CE (the coldest of  
589 the speleothem record) is related to a cataclysmic volcanic eruption that took place in Iceland in 536 CE  
590 and spewed ash across the Northern Hemisphere, together with the effect of two other massive eruptions in  
591 540 and 547 CE (Fig. 6b, Sigl et al., 2015). An unprecedented, long-lasting and spatially synchronized  
592 cooling was observed in European tree-ring records associated with these large volcanic eruptions,  
593 corresponding to the LALIA period (Büntgen et al., 2016). Therefore, volcanic events, at least the large  
594 ones such that from 536 CE in Iceland, have an effect driving temperature variations in the Pyrenean region.

595 There is also an evident synchrony between the European record and the Pyrenean speleothems in several  
596 of the more recent coldest intervals of the MCA and the LIA (dark blue bars in Fig. 6), probably a regional  
597 response to minima in solar irradiance as these events correspond to minima in sunspot numbers (Fig. 6c,  
598 (Usoskin et al., 2014, 2016): 1010-1050 CE (Oort minimum), 1280-1350 CE (Wolf minimum), 1450-1550  
599 CE (Spörer minimum), 1645-1715 CE (Maunder minimum) and 1790-1820 CE (Dalton minimum).  
600 Because variations in total solar irradiance are relatively small, on the order of a few tenths of  $\text{Wm}^{-2}$ , the  
601 mechanism that could result in a detectable cooling remains uncertain (Gray et al., 2010). While some  
602 studies discarded the idea that there has been a strong direct radiative influence of solar forcing on Northern  
603 Hemisphere temperatures in the past millennium (Schurer et al., 2014), other authors demonstrated a  
604 connection among solar variability and climate throughout changes in the large-scale atmospheric  
605 circulation of the Northern Hemisphere, such as the North Atlantic Oscillation (NAO) (Martin-Puertas et  
606 al., 2012). The NAO was proposed as a plausible mechanism to explain climate changes in Europe during  
607 the MCA vs LIA periods through the study in combination of proxy records and model simulations (Trouet  
608 et al., 2009; Mann et al., 2009). Thus, it was postulated that the MCA/LIA transition included a weakening  
609 of the Atlantic Meridional Overturning Circulation (AMOC) and a transition to more negative NAO  
610 conditions, resulting in a strong cooling of the North Atlantic region and an increase in the storm intensity  
611 (Trouet et al., 2012).

612 Such a connection among solar irradiance and temperature over Europe is then manifested through a change  
613 in the pressure gradient in the Atlantic that resembles a negative phase of the NAO and results in lower  
614 temperatures over Europe but also in a southward shift of the storm tracks enhancing precipitation amount  
615 over central and southern Europe (Swingedouw et al., 2011). As solar irradiance decreases, colder  
616 temperatures over the Northern Hemisphere continents are observed, especially in winter ( $1^\circ$  to  $2^\circ\text{C}$ ), in  
617 agreement with historical records and proxy data for surface temperatures (Shindell et al., 2001).

618 Coherently, most episodes of flooding in northwest and northern Europe region match with multi-decadal  
619 periods of grand solar minima and are thus also associated to the negative phase in the NAO index (Benito  
620 et al., 2015) (Fig. 6d).

621 In Iberia, the NAO index was embraced to explain the dryness during the MCA as observed in low  
622 resolution records (Moreno et al., 2012). Further studies based on proxy reconstructions in Iberia explained  
623 those MCA - LIA differences by using interactions between the NAO and the East Atlantic (EA) phases  
624 (Sánchez-López et al., 2016). In that line, the persistence of NAO phases, for example, the dominance of  
625 positive index during Medieval times, has been questioned (Ortega et al., 2015) and the interactions with  
626 other atmospheric modes, together with the non-stationary character of these atmospheric patterns, are  
627 nowadays important issues to contemplate when providing a NAO reconstruction (Comas-Bru and  
628 Hernández, 2018). In Fig. 6g, the NAO reconstruction provided using a lake record in NW Iberia  
629 (Hernández et al., 2020) is compared with the speleothem Pyrenean record demonstrating a good  
630 connection. Not surprisingly, the lack of correlation for some periods could be associated to i) chronological  
631 uncertainties of both records, ii) different season recorded by the analyzed proxies and iii) distinct influence  
632 of NAO in W and E of the IP.

## 633 **6. Conclusions**

634 The eight stalagmites presented in this study document for the first-time significant climate changes on the  
635 decadal scale in the Central Pyrenees during the last 2500 years. The  $\delta^{18}\text{O}$  composite record is dominated  
636 by regional temperature changes, as suggested by monitoring data and by the correlation with observational  
637 temperature data from the Pyrenees and at a hemispheric scale. The precipitation amount may also play a  
638 role as shown by the comparison with Pyrenean lake records.

639 On a regional scale, there is a good agreement with other Pyrenean and Iberian records (lake levels, tree  
640 rings and glacier advances) indicating a regional representativity of this new record. The RP stands out as  
641 a clear warm period, while the DA, MCA and LIA exhibit a high centennial-scale variability with cold  
642 (e.g., 520-540 CE and 1750-1850 CE) and warm intervals (e.g., 900-950 CE and 1150-1250 CE) modulated  
643 by increases and decreases in the precipitation amount, respectively. In spite temperature increases since  
644 1950 CE, known as the Great Acceleration within the IE, the last two decades are not the ones with the  
645 highest  $\delta^{18}\text{O}$  values in the composite record, likely pointing to the secondary role played by precipitation  
646 amount.

647 On a European scale, the Pyrenean composite is in robust agreement with the PAGES2k temperature  
648 reconstructions, particularly during warm events. It shows some similarities with other speleothem  
649 reconstructions from the Alps, Central and Northern Europe pointing to coherent patterns all over the  
650 continent for cold/wet and warm/dry periods of last 2500 years. This coherence is supported by synchronous  
651 changes with the sunspot number (low temperatures during solar minima), the North Atlantic Oscillation  
652 index (low NAO correlates with cold and wet decades) and major volcanic eruptions (e.g., several eruptions  
653 during LALIA).

654 **Author contribution.** MB, AM and CS designed the study; MB, AB and CS carried out the field work;  
655 MB, JH, IC, HS and NH did the analyses. LE and HC provided the U-Th facilities. MB and AM prepared  
656 the manuscript with contributions from all co-authors.

657 **Competing interests:** The authors declare that they have no conflict of interest.

658 **Acknowledgements.** We acknowledge the Spanish projects CTM2013-48639-C2-2-R (OPERA),  
659 CGL2016-77479-R (SPYRIT), and PID2019-106050RB-I00 (PYCACHU) for funding. We thank the  
660 Ordesa y Monte Perdido National Park (Spain) authorities and guards for their permission and help in  
661 exploring and monitoring the studied caves. We also thank Jaime Mas and Xavier Fuertes (Free Caving  
662 Team and GEB), Ramón Queraltó and Carles Pons (Asociación Científica Espeleológica Cotiella), Maria  
663 Leunda and the Palazzo family ([www.hotelpalazio.com](http://www.hotelpalazio.com)) for their invaluable help during fieldwork. Dr.

664 Miguel Sevilla (IPE-CSIC) is greatly acknowledge for his design and production of maps in Fig. 1. The  
665 authors would like to acknowledge the use of the Servicio General de Apoyo a la Investigación-SAI,  
666 University of Zaragoza. This study contributes to the work carried out by the DGA research group Procesos  
667 Geoambientales y Cambio Global (ref.: E02-20R). Miguel Bartolomé is supported by the HORIZON TMA  
668 MSCA Postdoctoral Fellowships - Global Fellowships 2022 MODKARST project (n° 101107943) funded  
669 by the European Union. Isabel Cacho thanks the Catalan Institution for Research and Advanced Studies  
670 (ICREA) academia program from the Generalitat de Catalunya.

## 671 **References**

672 Abrantes, F., Rodrigues, T., Rufino, M., Salgueiro, E., Oliveira, D., Gomes, S., Oliveira, P., Costa,  
673 A., Mil-Homens, M., Drago, T., and Naughton, F.: The climate of the Common Era off the  
674 Iberian Peninsula, *Clim. Past*, 13, 1901–1918, <https://doi.org/10.5194/cp-13-1901-2017>, 2017.

675 Affolter, S., Häuselmann, A., Fleitmann, D., Edwards, R. L., Cheng, H., and Leuenberger, M.:  
676 Central Europe temperature constrained by speleothem fluid inclusion water isotopes over the  
677 past 14,000 years, *Science Advances*, 5, eaav3809, <https://doi.org/10.1126/sciadv.aav3809>,  
678 2019.

679 Ahmed, M., Anchukaitis, K. J., Asrat, A., Borgaonkar, H. P., Braidia, M., Buckley, B. M., Büntgen,  
680 U., Chase, B. M., Christie, D. A., Cook, E. R., Curran, M. A. J., Diaz, H. F., Esper, J., Fan, Z.-X.,  
681 Gaire, N. P., Ge, Q., Gergis, J., González-Rouco, J. F., Goosse, H., Grab, S. W., Graham, N.,  
682 Graham, R., Grosjean, M., Hanhijärvi, S. T., Kaufman, D. S., Kiefer, T., Kimura, K., Korhola, A. A.,  
683 Krusic, P. J., Lara, A., Lézine, A.-M., Ljungqvist, F. C., Lorrey, A. M., Luterbacher, J., Masson-  
684 Delmotte, V., McCarroll, D., McConnell, J. R., McKay, N. P., Morales, M. S., Moy, A. D.,  
685 Mulvaney, R., Mundo, I. A., Nakatsuka, T., Nash, D. J., Neukom, R., Nicholson, S. E., Oerter, H.,  
686 Palmer, J. G., Phipps, S. J., Prieto, M. R., Rivera, A., Sano, M., Severi, M., Shanahan, T. M., Shao,  
687 X., Shi, F., Sigl, M., Smerdon, J. E., Solomina, O. N., Steig, E. J., Stenni, B., Thamban, M., Trouet,  
688 V., Turney, C. S. M., Umer, M., van Ommen, T., Verschuren, D., Viau, A. E., Villalba, R., Vinther,  
689 B. M., von Gunten, L., Wagner, S., Wahl, E. R., Wanner, H., Werner, J. P., White, J. W. C., Yasue,  
690 K., Zorita, E., and PAGES 2k Consortium: Continental-scale temperature variability during the  
691 past two millennia, *Nature Geoscience*, 6, 339–346, <https://doi.org/10.1038/ngeo1797>, 2013.

692 Ait Brahim, Y., Wassenburg, J. A., Sha, L., Cruz, F. W., Deininger, M., Sifeddine, A., Bouchaou, L.,  
693 Spötl, C., Edwards, R. L., and Cheng, H.: North Atlantic Ice-Rafting, Ocean and Atmospheric  
694 Circulation During the Holocene: Insights From Western Mediterranean Speleothems,  
695 *Geophysical Research Letters*, 46, 7614–7623, <https://doi.org/10.1029/2019GL082405>, 2019.

696 Baker, A., C. Hellstrom, J., Kelly, B. F. J., Mariethoz, G., and Trouet, V.: A composite annual-  
697 resolution stalagmite record of North Atlantic climate over the last three millennia, *Sci Rep*, 5,  
698 10307, <https://doi.org/10.1038/srep10307>, 2015.

699 Bard, E., Raisbeck, G., Yiou, F., and Jouzel, J.: Solar irradiance during the last 1200 years based  
700 on cosmogenic nuclides, *Tellus B*, 52, 985–992, <https://doi.org/10.1034/j.1600-0889.2000.d01-7.x>, 2000.

702 Bartolomé, M.: La Cueva del Caserío de Sesó (Pirineo Central): espeleogénesis, dinámica actual  
703 y reconstrucción paleoambiental de los últimos 13.000 años, Universidad de Zaragoza, 276 pp.,  
704 2016.

705 Bartolomé, M., Moreno, A., Sancho, C., Stoll, H. M., Cacho, I., Spötl, C., Belmonte, Á., Edwards,  
706 R. L., Cheng, H., and Hellstrom, J. C.: Hydrological change in Southern Europe responding to

707 increasing North Atlantic overturning during Greenland Stadial 1, *PNAS*, 112, 6568–6572,  
708 <https://doi.org/10.1073/pnas.1503990112>, 2015a.

709 Bartolomé, M., Sancho, C., Moreno, A., Oliva-Urcia, B., Belmonte, Á., Bastida, J., Cheng, H., and  
710 Edwards, R. L.: Upper Pleistocene interstratal piping-cave speleogenesis: The Seso Cave System  
711 (Central Pyrenees, Northern Spain), *Geomorphology*, 228, 335–344,  
712 <https://doi.org/10.1016/j.geomorph.2014.09.007>, 2015b.

713 Beniston, M., Farinotti, D., Stoffel, M., Andreassen, L. M., Coppola, E., Eckert, N., Fantini, A.,  
714 Giacona, F., Hauck, C., Huss, M., Huwald, H., Lehning, M., López-Moreno, J.-I., Magnusson, J.,  
715 Marty, C., Morán-Tejeda, E., Morin, S., Naaim, M., Provenzale, A., Rabatel, A., Six, D., Stötter,  
716 J., Strasser, U., Terzago, S., and Vincent, C.: The European mountain cryosphere: a review of its  
717 current state, trends, and future challenges, *The Cryosphere*, 12, 759–794,  
718 <https://doi.org/10.5194/tc-12-759-2018>, 2018.

719 Benito, G., Macklin, M. G., Panin, A., Rossato, S., Fontana, A., Jones, A. F., Machado, M. J.,  
720 Matlakhova, E., Mozzi, P., and Zielhofer, C.: Recurring flood distribution patterns related to  
721 short-term Holocene climatic variability, *Sci Rep*, 5, 16398, <https://doi.org/10.1038/srep16398>,  
722 2015.

723 Bernal-Wormull, J. L., Moreno, A., Pérez-Mejías, C., Bartolomé, M., Aranburu, A.,  
724 Arriolabengoa, M., Iriarte, E., Cacho, I., Spötl, C., Edwards, R. L., and Cheng, H.: Immediate  
725 temperature response in northern Iberia to last deglacial changes in the North Atlantic,  
726 *Geology*, <https://doi.org/10.1130/G48660.1>, 2021.

727 Bücher, A. and Dessens, J.: Secular Trend of Surface Temperature at an Elevated Observatory  
728 in the Pyrenees, *Journal of Climate*, 4, 859–868, [https://doi.org/10.1175/1520-0442\(1991\)004<0859:STOSTA>2.0.CO;2](https://doi.org/10.1175/1520-0442(1991)004<0859:STOSTA>2.0.CO;2), 1991.

730 Büntgen, U., Tegel, W., Nicolussi, K., McCormick, M., Frank, D., Trouet, V., Kaplan, J. O., Herzig,  
731 F., Heussner, K.-U., Wanner, H., Luterbacher, J., and Esper, J.: 2500 Years of European Climate  
732 Variability and Human Susceptibility, *Science*, 2011.

733 Büntgen, U., Myglan, V. S., Ljungqvist, F. C., McCormick, M., Di Cosmo, N., Sigl, M., Jungclaus,  
734 J., Wagner, S., Krusic, P. J., Esper, J., Kaplan, J. O., de Vaan, M. A. C., Luterbacher, J., Wacker, L.,  
735 Tegel, W., and Kiryandov, A. V.: Cooling and societal change during the Late Antique Little Ice  
736 Age from 536 to around 660 AD, *Nature Geosci*, 9, 231–236,  
737 <https://doi.org/10.1038/ngeo2652>, 2016.

738 Büntgen, U., Krusic, P. J., Verstege, A., Sangüesa-Barreda, G., Wagner, S., Camarero, J. J.,  
739 Ljungqvist, F. C., Zorita, E., Oppenheimer, C., Konter, O., Tegel, W., Gärtner, H., Cherubini, P.,  
740 Reinig, F., and Esper, J.: New Tree-Ring Evidence from the Pyrenees Reveals Western  
741 Mediterranean Climate Variability since Medieval Times, *J. Climate*, 30, 5295–5318,  
742 <https://doi.org/10.1175/JCLI-D-16-0526.1>, 2017.

743 Büntgen, U., Urban, O., Krusic, P. J., Rybníček, M., Kolář, T., Kyncl, T., Ač, A., Koňasová, E.,  
744 Čáslavský, J., Esper, J., Wagner, S., Saurer, M., Tegel, W., Dobrovolný, P., Cherubini, P., Reinig,  
745 F., and Trnka, M.: Recent European drought extremes beyond Common Era background  
746 variability, *Nat. Geosci.*, 14, 190–196, <https://doi.org/10.1038/s41561-021-00698-0>, 2021.

747 Cisneros, M., Cacho, I., Frigola, J., Canals, M., Masqué, P., Martrat, B., Casado, M., Grimalt, J.  
748 O., Pena, L. D., Margaritelli, G., and Lirer, F.: Sea surface temperature variability in the central-



- 749 western Mediterranean Sea during the last 2700 years: a multi-proxy and multi-record  
750 approach, *Clim. Past*, 12, 849–869, <https://doi.org/10.5194/cp-12-849-2016>, 2016.
- 751 Cisneros, M., Cacho, I., Moreno, A., Stoll, H., Torner, J., Català, A., Edwards, R. L., Cheng, H.,  
752 and Fornós, J. J.: Hydroclimate variability during the last 2700 years based on stalagmite multi-  
753 proxy records in the central-western Mediterranean, *Quaternary Science Reviews*, 269,  
754 107137, <https://doi.org/10.1016/j.quascirev.2021.107137>, 2021.
- 755 Comas-Bru, L. and Hernández, A.: Reconciling North Atlantic climate modes: revised monthly  
756 indices for the East Atlantic and the Scandinavian patterns beyond the 20th century, *Earth  
757 System Science Data*, 10, 2329–2344, <https://doi.org/10.5194/essd-10-2329-2018>, 2018.
- 758 Comas-Bru, L., Rehfeld, K., Roesch, C., Amirnezhad-Mozhdehi, S., Harrison, S. P.,  
759 Atsawawaranunt, K., Ahmad, S. M., Brahim, Y. A., Baker, A., Bosomworth, M., Breitenbach, S.  
760 F. M., Burstyn, Y., Columbu, A., Deininger, M., Demény, A., Dixon, B., Fohlmeister, J., Hatvani, I.  
761 G., Hu, J., Kaushal, N., Kern, Z., Labuhn, I., Lechleitner, F. A., Lorrey, A., Martrat, B., Novello, V.  
762 F., Oster, J., Pérez-Mejías, C., Scholz, D., Scroxton, N., Sinha, N., Ward, B. M., Warken, S.,  
763 Zhang, H., and SISAL Working Group members: SISALv2: a comprehensive speleothem isotope  
764 database with multiple age–depth models, *Earth System Science Data*, 12, 2579–2606,  
765 <https://doi.org/10.5194/essd-12-2579-2020>, 2020.
- 766 Corella, J. P., Valero-Garcés, B. L., Vicente-Serrano, S. M., Brauer, A., and Benito, G.: Three  
767 millennia of heavy rainfalls in Western Mediterranean: frequency, seasonality and atmospheric  
768 drivers, *Scientific Reports*, 6, <https://doi.org/10.1038/srep38206>, 2016.
- 769 Dessens, J. and Bücher, A.: Changes in minimum and maximum temperatures at the Pic du  
770 Midi in relation with humidity and cloudiness, 1882–1984, *Atmospheric Research*, 37, 147–  
771 162, [https://doi.org/10.1016/0169-8095\(94\)00075-O](https://doi.org/10.1016/0169-8095(94)00075-O), 1995.
- 772 Edwards, R. L., Chen, J. H., and Wasserburg, G. J.: 238U-234U-230Th-232Th systematics and  
773 the precise measurements of time over the past 500.000 years, *Earth and Planetary Science  
774 Letters*, 81, 175–192, 1987.
- 775 Fohlmeister, J.: A statistical approach to construct composite climate records of dated  
776 archives, *Quaternary Geochronology*, 14, 48–56,  
777 <https://doi.org/10.1016/j.quageo.2012.06.007>, 2012.
- 778 Fohlmeister, J., Kromer, B., and Mangini, A.: The influence of soil organic matter age spectrum  
779 on the reconstruction of atmospheric 14C levels via stalagmites, *Radiocarbon*, 53, 99–115,  
780 <https://doi.org/10.1017/S003382220003438X>, 2011.
- 781 Fohlmeister, J., Schröder-Ritzrau, A., Scholz, D., Spötl, C., Riechelmann, D. F. C., Mudelsee, M.,  
782 Wackerbarth, A., Gerdes, A., Riechelmann, S., Immenhauser, A., Richter, D. K., and Mangini, A.:  
783 Bunker Cave stalagmites: an archive for central European Holocene climate variability, *Clim.  
784 Past*, 8, 1751–1764, <https://doi.org/10.5194/cp-8-1751-2012>, 2012.
- 785 García-Ruiz, J. M., Palacios, D., Andrés, N. de, Valero-Garcés, B. L., López-Moreno, J. I., and  
786 Sanjuán, Y.: Holocene and ‘Little Ice Age’ glacial activity in the Marboré Cirque, Monte Perdido  
787 Massif, Central Spanish Pyrenees, *The Holocene*, 24, 1439–1452,  
788 <https://doi.org/10.1177/0959683614544053>, 2014.
- 789 Genty, D., Vokal, B., Obelic, B., and Massault, M.: Bomb 14C time history recorded in two  
790 modern stalagmites — importance for soil organic matter dynamics and bomb 14C distribution

791 over continents, *Earth and Planetary Science Letters*, 160, 795–809,  
792 [https://doi.org/10.1016/S0012-821X\(98\)00128-9](https://doi.org/10.1016/S0012-821X(98)00128-9), 1998.

793 Genty, D., Blamart, D., Ghaleb, B., Plagnes, V., Causse, Ch., Bakalowicz, M., Zouari, K., Chkir, N.,  
794 Hellstrom, J., Wainer, K., and Bourges, F.: Timing and dynamics of the last deglaciation from  
795 European and North African  $\delta^{13}\text{C}$  stalagmite profiles—comparison with Chinese and South  
796 Hemisphere stalagmites, *Quaternary Science Reviews*, 25, 2118–2142,  
797 <https://doi.org/10.1016/j.quascirev.2006.01.030>, 2006.

798 Genty, D., Labuhn, I., Hoffmann, G., Danis, P. A., Mestre, O., Bourges, F., Wainer, K., Massault,  
799 M., Van Exter, S., Régnier, E., Orengo, Ph., Falourd, S., and Minster, B.: Rainfall and cave water  
800 isotopic relationships in two South-France sites, *Geochimica et Cosmochimica Acta*, 131, 323–  
801 343, <https://doi.org/10.1016/j.gca.2014.01.043>, 2014.

802 Giménez, R., Bartolomé, M., Gázquez, F., Iglesias, M., and Moreno, A.: Underlying Climate  
803 Controls in Triple Oxygen ( $^{16}\text{O}$ ,  $^{17}\text{O}$ ,  $^{18}\text{O}$ ) and Hydrogen ( $^1\text{H}$ ,  $^2\text{H}$ ) Isotopes Composition of  
804 Rainfall (Central Pyrenees), *Front. Earth Sci.*, 9, <https://doi.org/10.3389/feart.2021.633698>,  
805 2021.

806 González-Sampériz, P., Aranbarri, J., Pérez-Sanz, A., Gil-Romera, G., Moreno, A., Leunda, M.,  
807 Sevilla-Callejo, M., Corella, J. P., Morellón, M., Oliva, B., and Valero-Garcés, B.: Environmental  
808 and climate change in the southern Central Pyrenees since the Last Glacial Maximum: A view  
809 from the lake records, *CATENA*, 149, 668–688, 2017.

810 Goosse, H., Guiot, J., Mann, M. E., Dubinkina, S., and Sallaz-Damaz, Y.: The medieval climate  
811 anomaly in Europe: Comparison of the summer and annual mean signals in two  
812 reconstructions and in simulations with data assimilation, *Global and Planetary Change*, 84–85,  
813 35–47, <https://doi.org/10.1016/j.gloplacha.2011.07.002>, 2012.

814 Gray, L. J., Beer, J., Geller, M., Haigh, J. D., Lockwood, M., Matthes, K., Cubasch, U., Fleitmann,  
815 D., Harrison, G., Hood, L., Luterbacher, J., Meehl, G. A., Shindell, D., van Geel, B., and White,  
816 W.: Solar influences on climate, *Rev. Geophys.*, 48, RG4001, 2010.

817 Hammer, O., Harper, D. A. T., and Ryan, P. D.: PAST: Paleontological statistics software package  
818 for education and data analysis. 4(1): 9pp., *Palaeontologia Electronica*, 4 (1), 9, 2001.

819 Helama, S., Meriläinen, J., and Tuomenvirta, H.: Multicentennial megadrought in northern  
820 Europe coincided with a global El Niño–Southern Oscillation drought pattern during the  
821 Medieval Climate Anomaly, *Geology*, 37, 175–178, <https://doi.org/10.1130/G25329A.1>, 2009.

822 Hellstrom, J.: U–Th dating of speleothems with high initial  $^{230}\text{Th}$  using stratigraphical  
823 constraint, *Quaternary Geochronology*, 1, 289–295,  
824 <https://doi.org/10.1016/j.quageo.2007.01.004>, 2006.

825 Hernández, A., Sánchez-López, G., Pla-Rabes, S., Comas-Bru, L., Parnell, A., Cahill, N., Geyer, A.,  
826 Trigo, R. M., and Giral, S.: A 2,000-year Bayesian NAO reconstruction from the Iberian  
827 Peninsula, *Sci Rep*, 10, 14961, <https://doi.org/10.1038/s41598-020-71372-5>, 2020.

828 Holzhauser, H., Magny, M., and Zumbühl, H. J.: Glacier and lake-level variations in west-  
829 central Europe over the last 3500 years:, *The Holocene*,  
830 <https://doi.org/10.1191/0959683605hl853ra>, 2016.

- 831 Hu, H.-M., Michel, V., Valensi, P., Mii, H.-S., Starnini, E., Zunino, M., and Shen, C.-C.: Stalagmite-  
832 Inferred Climate in the Western Mediterranean during the Roman Warm Period, *Climate*, 10,  
833 93, <https://doi.org/10.3390/cli10070093>, 2022.
- 834 Hua, Q., McDonald, J., Redwood, D., Drysdale, R., Lee, S., Fallon, S., and Hellstrom, J.: Robust  
835 chronological reconstruction for young speleothems using radiocarbon, *Quaternary*  
836 *Geochronology*, 14, 67–80, <https://doi.org/10.1016/j.quageo.2012.04.017>, 2012.
- 837 Hua, Q., Cook, D., Fohlmeister, J., Penny, D., Bishop, P., and Buckman, S.: Radiocarbon Dating  
838 of a Speleothem Record of Paleoclimate for Angkor, Cambodia, *Radiocarbon*, 59, 1873–1890,  
839 <https://doi.org/10.1017/RDC.2017.115>, 2017.
- 840 Hughes, P. D.: Little Ice Age glaciers and climate in the Mediterranean mountains: a new  
841 analysis, *CIG*, 44, 15, <https://doi.org/10.18172/cig.3362>, 2018.
- 842 Ilyashuk, E. A., Heiri, O., Ilyashuk, B. P., Koinig, K. A., and Psenner, R.: The Little Ice Age  
843 signature in a 700-year high-resolution chironomid record of summer temperatures in the  
844 Central Eastern Alps, *Clim Dyn*, 52, 6953–6967, <https://doi.org/10.1007/s00382-018-4555-y>,  
845 2019.
- 846 IPCC, 2021: Climate Change 2021: The Physical Science Basis. Contribution of Working Group I  
847 to the Sixth Assessment Report of the Intergovernmental Panel on Climate Change [Masson-  
848 Delmotte, V., P. Zhai, A. Pirani, S.L. Connors, C. Péan, S. Berger, N. Caud, Y. Chen, L. Goldfarb,  
849 M.I. Gomis, M. Huang, K. Leitzell, E. Lonnoy, J.B.R. Matthews, T.K. Maycock, T. Waterfield, O.  
850 Yelekçi, R. Yu, and B. Zhou (eds.)]. Cambridge University Press, Cambridge, United Kingdom  
851 and New York, NY, USA, 2391 pp.[doi:10.1017/9781009157896](https://doi.org/10.1017/9781009157896).
- 852 Jacob, D., Kotova, L., Teichmann, C., Sobolowski, S. P., Vautard, R., Donnelly, C., Koutroulis, A.  
853 G., Grillakis, M. G., Tsanis, I. K., Damm, A., Sakalli, A., and van Vliet, M. T. H.: Climate Impacts in  
854 Europe Under +1.5°C Global Warming, *Earth’s Future*, 6, 264–285,  
855 <https://doi.org/10.1002/2017EF000710>, 2018.
- 856 Jiménez-Moreno, G., García-Alix, A., Hernández-Corbalán, M. D., Anderson, R. S., and Delgado-  
857 Huertas, A.: Vegetation, fire, climate and human disturbance history in the southwestern  
858 Mediterranean area during the late Holocene, *Quaternary Research*, 79, 110–122,  
859 <https://doi.org/10.1016/j.yqres.2012.11.008>, 2013.
- 860 Konecky, B. L., McKay, N. P., Churakova (Sidorova), O. V., Comas-Bru, L., Dassié, E. P., DeLong,  
861 K. L., Falster, G. M., Fischer, M. J., Jones, M. D., Jonkers, L., Kaufman, D. S., Leduc, G.,  
862 Managave, S. R., Martrat, B., Opel, T., Orsi, A. J., Partin, J. W., Sayani, H. R., Thomas, E. K.,  
863 Thompson, D. M., Tyler, J. J., Abram, N. J., Atwood, A. R., Conroy, J. L., Kern, Z., Porter, T. J.,  
864 Stevenson, S. L., von Gunten, L., and the Iso2k Project Members: The Iso2k Database: A global  
865 compilation of paleo- $\delta^{18}\text{O}$  and  $\delta^2\text{H}$  records to aid understanding of Common Era climate, *Earth*  
866 *System Science Data Discussions*, 1–49, <https://doi.org/10.5194/essd-2020-5>, 2020.
- 867 Lachniet, M. S.: Climatic and environmental controls on speleothem oxygen-isotope values,  
868 *Quaternary Science Reviews*, 28, 412–432, 2009.
- 869 Leunda, M., González-Sampériz, P., Gil-Romera, G., Bartolomé, M., Belmonte-Ribas, Á., Gómez-  
870 García, D., Kaltenrieder, P., Rubiales, J. M., Schwörer, C., Tinner, W., Morales-Molino, C., and  
871 Sancho, C.: Ice cave reveals environmental forcing of long-term Pyrenean tree line dynamics,  
872 *Journal of Ecology*, 107, 814–828, <https://doi.org/10.1111/1365-2745.13077>, 2019.

- 873 López-Moreno, J. I., Revuelto, J., Rico, I., Chueca-Cía, J., Julián, A., Serreta, A., Serrano, E.,  
874 Vicente-Serrano, S. M., Azorin-Molina, C., Alonso-González, E., and García-Ruiz, J. M.: Thinning  
875 of the Monte Perdido Glacier in the Spanish Pyrenees since 1981, *The Cryosphere*, 10, 681–  
876 694, <https://doi.org/10.5194/tc-10-681-2016>, 2016.
- 877 López-Moreno, J. I., García-Ruiz, J. M., Vicente-Serrano, S. M., Alonso-González, E., Revuelto-  
878 Benedí, J., Rico, I., Izagirre, E., and Beguería-Portugués, S.: Critical discussion of: “A farewell to  
879 glaciers: Ecosystem services loss in the Spanish Pyrenees,” *Journal of Environmental*  
880 *Management*, 275, 111247, <https://doi.org/10.1016/j.jenvman.2020.111247>, 2020.
- 881 Lüning, S., Schulte, L., Garcés-Pastor, S., Danladi, I. b., and Gałka, M.: The Medieval Climate  
882 Anomaly in the Mediterranean Region, *Paleoceanography and Paleoclimatology*, 34, 1625–  
883 1649, <https://doi.org/10.1029/2019PA003734>, 2019.
- 884 Luterbacher, J., Werner, J. P., Smerdon, J. E., Fernández-Donado, L., González-Rouco, F. J.,  
885 Barriopedro, D., Ljungqvist, F. C., Büntgen, U., Zorita, E., Wagner, S., Esper, J., McCarroll, D.,  
886 Toreti, A., Frank, D., Jungclaus, J. H., M Barriendos, Bertolin, C., Bothe, O., Brázdil, R., Camuffo,  
887 D., Dobrovolný, P., Gagen, M., García-Bustamante, E., Ge, Q., Gómez-Navarro, J. J., Guiot, J.,  
888 Hao, Z., Hegerl, G. C., Holmgren, K., Klimenko, V. V., Martín-Chivelet, J., Pfister, C., N Roberts,  
889 Schindler, A., Schurer, A., Solomina, O., Gunten, L. von, Wahl, E., Wanner, H., Wetter, O.,  
890 Xoplaki, E., Yuan, N., D Zanchettin, Zhang, H., and Zerefos, C.: European summer temperatures  
891 since Roman times, *Environ. Res. Lett.*, 11, 024001, [https://doi.org/10.1088/1748-](https://doi.org/10.1088/1748-9326/11/2/024001)  
892 [9326/11/2/024001](https://doi.org/10.1088/1748-9326/11/2/024001), 2016.
- 893 Magny, M.: Orbital, ice-sheet, and possible solar forcing of Holocene lake-level fluctuations in  
894 west-central Europe: A comment on Bleicher, *The Holocene*,  
895 <https://doi.org/10.1177/0959683613483627>, 2013.
- 896 Mangini, A., Spötl, C., and Verdes, P.: Reconstruction of temperature in the Central Alps during  
897 the past 2000 yr from a  $\delta^{18}\text{O}$  stalagmite record, *Earth and Planetary Science Letters*, 235, 741–  
898 751, <https://doi.org/10.1016/j.epsl.2005.05.010>, 2005.
- 899 Mann, M. E.: Beyond the hockey stick: Climate lessons from the Common Era, *PNAS*, 118,  
900 <https://doi.org/10.1073/pnas.2112797118>, 2021.
- 901 Mann, M. E., Zhang, Z., Rutherford, S., Bradley, R. S., Hughes, M. K., Shindell, D., Ammann, C.,  
902 Faluvegi, G., and Ni, F.: Global Signatures and Dynamical Origins of the Little Ice Age and  
903 Medieval Climate Anomaly, *Science*, 326, 1256–1260, 2009.
- 904 Margaritelli, G., Cacho, I., Català, A., Barra, M., Bellucci, L. G., Lubritto, C., Rettori, R., and Lirer,  
905 F.: Persistent warm Mediterranean surface waters during the Roman period, *Sci Rep*, 10,  
906 10431, <https://doi.org/10.1038/s41598-020-67281-2>, 2020.
- 907 Markowska, M., Fohlmeister, J., Treble, P. C., Baker, A., Andersen, M. S., and Hua, Q.:  
908 Modelling the 14C bomb-pulse in young speleothems using a soil carbon continuum model,  
909 *Geochimica et Cosmochimica Acta*, 261, 342–367, <https://doi.org/10.1016/j.gca.2019.04.029>,  
910 2019.
- 911 Martín-Chivelet, J., Muñoz-García, M. B., Edwards, R. L., Turrero, M. J., and Ortega, A. I.: Land  
912 surface temperature changes in Northern Iberia since 4000yrBP, based on  $\delta^{13}\text{C}$  of  
913 speleothems, *Global and Planetary Change*, 77, 1–12,  
914 <https://doi.org/10.1016/j.gloplacha.2011.02.002>, 2011.

- 915 Martín-Puertas, C., Valero-Garcés, B. L., Brauer, A., Mata, M. P., Delgado-Huertas, A., and  
 916 Dulski, P.: The Iberian-Roman Humid Period (2600-1600 cal yr BP) in the Zoñar Lake varve  
 917 record (Andalucía, southern Spain), *Quaternary Research*, 71, 108–120, 2009.
- 918 Martín-Puertas, C., Matthes, K., Brauer, A., Muscheler, R., Hansen, F., Petrick, C., Aldahan, A.,  
 919 Possnert, G., and van Geel, B.: Regional atmospheric circulation shifts induced by a grand solar  
 920 minimum, *Nature Geoscience*, <https://doi.org/10.1038/ngeo1460>, 2012.
- 921 McCormick, M., Büntgen, U., Cane, M. A., Cook, E. R., Harper, K., Huybers, P., Litt, T., Manning,  
 922 S. W., Mayewski, P. A., More, A. F. M., Nicolussi, K., and Tegel, W.: Climate Change during and  
 923 after the Roman Empire: Reconstructing the Past from Scientific and Historical Evidence, *The  
 924 Journal of Interdisciplinary History*, 43, 169–220, [https://doi.org/10.1162/JINH\\_a\\_00379](https://doi.org/10.1162/JINH_a_00379), 2012.
- 925 Morellón, M., Valero-Garcés, B., Vegas-Vilarrúbia, T., González-Sampérez, P., Romero, Ó.,  
 926 Delgado-Huertas, A., Mata, P., Moreno, A., Rico, M., and Corella, J. P.: Lateglacial and Holocene  
 927 palaeohydrology in the western Mediterranean region: The Lake Estanya record (NE Spain),  
 928 *Quaternary Science Reviews*, 28, 2582–2599, 2009.
- 929 Morellón, M., Valero-Garcés, B., González-Sampérez, P., Vegas-Vilarrúbia, T., Rubio, E.,  
 930 Rieradevall, M., Delgado-Huertas, A., Mata, P., Romero, Ó., Engstrom, D. R., López-Vicente, M.,  
 931 Navas, A., and Soto, J.: Climate changes and human activities recorded in the sediments of  
 932 Lake Estanya (NE Spain) during the Medieval Warm Period and Little Ice Age, *Journal of  
 933 Paleolimnology*, 46, 423–452, <https://doi.org/10.1007/s10933-009-9346-3>, 2011.
- 934 Morellón, M., Pérez-Sanz, A., Corella, J. P., Büntgen, U., Catalán, J., González-Sampérez, P.,  
 935 González-Trueba, J. J., López-Sáez, J. A., Moreno, A., Pla-Rabes, S., Saz-Sánchez, M. Á.,  
 936 Scussolini, P., Serrano, E., Steinhilber, F., Stefanova, V., Vegas-Vilarrúbia, T., and Valero-Garcés,  
 937 B.: A multi-proxy perspective on millennium-long climate variability in the Southern Pyrenees,  
 938 *Clim. Past*, 8, 683–700, <https://doi.org/10.5194/cp-8-683-2012>, 2012.
- 939 Moreno, A., Stoll, H. M., Jiménez-Sánchez, M., Cacho, I., Valero-Garcés, B., Ito, E., and Edwards,  
 940 L. R.: A speleothem record of rapid climatic shifts during last glacial period from Northern  
 941 Iberian Peninsula, *Global and Planetary Change*, 71, 218–231;  
 942 [doi:10.1016/j.gloplacha.2009.10.002](https://doi.org/10.1016/j.gloplacha.2009.10.002), 2010.
- 943 Moreno, A., Pérez, A., Frigola, J., Nieto-Moreno, V., Rodrigo-Gámiz, M., Martrat, B., González-  
 944 Sampérez, P., Morellón, M., Martín-Puertas, C., Corella, J. P., Belmonte, Á., Sancho, C., Cacho, I.,  
 945 Herrera, G., Canals, M., Grimalt, J. O., Jiménez-Espejo, F., Martínez-Ruiz, F., Vegas-Vilarrúbia,  
 946 T., and Valero-Garcés, B. L.: The Medieval Climate Anomaly in the Iberian Peninsula  
 947 reconstructed from marine and lake records, *Quaternary Science Reviews*, 43, 16–32,  
 948 <https://doi.org/10.1016/j.quascirev.2012.04.007>, 2012.
- 949 Moreno, A., Sancho, C., Bartolomé, M., Oliva-Urcia, B., Delgado-Huertas, A., Estrela, M. J.,  
 950 Corell, D., López-Moreno, J. I., and Cacho, I.: Climate controls on rainfall isotopes and their  
 951 effects on cave drip water and speleothem growth: the case of Molinos cave (Teruel, NE  
 952 Spain), *Clim Dyn*, 43, 221–241, <https://doi.org/10.1007/s00382-014-2140-6>, 2014.
- 953 Moreno, A., Pérez-Mejías, C., Bartolomé, M., Sancho, C., Cacho, I., Stoll, H., Delgado-Huertas,  
 954 A., Hellstrom, J., Edwards, R. L., and Cheng, H.: New speleothem data from Molinos and Ejulve  
 955 caves reveal Holocene hydrological variability in northeast Iberia, *Quaternary Research*, 1–11,  
 956 <https://doi.org/10.1017/qua.2017.39>, 2017.

957 Moreno, A., Iglesias, M., Azorin-Molina, C., Pérez-Mejías, C., Bartolomé, M., Sancho, C., Stoll,  
958 H., Cacho, I., Frigola, J., Osácar, C., Muñoz, A., Delgado-Huertas, A., Blade, I., and Vimeux, F.:  
959 Spatial variability of northern Iberian rainfall stable isotope values: Investigating climatic  
960 controls on daily and monthly timescales, *Atmospheric Chemistry and Physics Discussions*, 1–  
961 34, <https://doi.org/10.5194/acp-2020-861>, 2021a.

962 Moreno, A., Bartolomé, M., López-Moreno, J. I., Pey, J., Corella, J. P., García-Orellana, J.,  
963 Sancho, C., Leunda, M., Gil-Romera, G., González-Sampériz, P., Pérez-Mejías, C., Navarro, F.,  
964 Otero-García, J., Lapazaran, J., Alonso-González, E., Cid, C., López-Martínez, J., Oliva-Urcia, B.,  
965 Faria, S. H., Sierra, M. J., Millán, R., Querol, X., Alastuey, A., and García-Ruiz, J. M.: The case of a  
966 southern European glacier which survived Roman and medieval warm periods but is  
967 disappearing under recent warming, *The Cryosphere*, 15, 1157–1172,  
968 <https://doi.org/10.5194/tc-15-1157-2021>, 2021b.

969 Morice, C. P., Kennedy, J. J., Rayner, N. A., Winn, J. P., Hogan, E., Killick, R. E., Dunn, R. J. H.,  
970 Osborn, T. J., Jones, P. D., and Simpson, I. R.: An Updated Assessment of Near-Surface  
971 Temperature Change From 1850: The HadCRUT5 Data Set, *Journal of Geophysical Research:*  
972 *Atmospheres*, 126, e2019JD032361, <https://doi.org/10.1029/2019JD032361>, 2021.

973 Naumann, G., Cammalleri, C., Mentaschi, L., and Feyen, L.: Increased economic drought  
974 impacts in Europe with anthropogenic warming, *Nat. Clim. Chang.*, 11, 485–491,  
975 <https://doi.org/10.1038/s41558-021-01044-3>, 2021.

976 Neukom, R., Steiger, N., Gómez-Navarro, J. J., Wang, J., and Werner, J. P.: No evidence for  
977 globally coherent warm and cold periods over the preindustrial Common Era, *Nature*, 571,  
978 550–554, <https://doi.org/10.1038/s41586-019-1401-2>, 2019.

979 Observatorio Pirenaico de Cambio Global: Executive summary report OPCC2: Climate change in  
980 the Pyrenees: impacts, vulnerability and adaptation, 2018.

981 Oliva, M., Ruiz-Fernández, J., Barriendos, M., Benito, G., Cuadrat, J. M., Domínguez-Castro, F.,  
982 García-Ruiz, J. M., Giralt, S., Gómez-Ortiz, A., Hernández, A., López-Costas, O., López-Moreno,  
983 J. I., López-Sáez, J. A., Martínez-Cortizas, A., Moreno, A., Prohom, M., Saz, M. A., Serrano, E.,  
984 Tejedor, E., Trigo, R., Valero-Garcés, B., and Vicente-Serrano, S. M.: The Little Ice Age in Iberian  
985 mountains, *Earth-Science Reviews*, 177, 175–208,  
986 <https://doi.org/10.1016/j.earscirev.2017.11.010>, 2018.

987 Ortega, P., Lehner, F., Swingedouw, D., Masson-Delmotte, V., Raible, C. C., Casado, M., and  
988 Yiou, P.: A model-tested North Atlantic Oscillation reconstruction for the past millennium,  
989 *Nature*, 523, 71–74, <https://doi.org/10.1038/nature14518>, 2015.

990 PAGES 2k Consortium: Continental-scale temperature variability during the past two millennia,  
991 *Nature Geosci*, 6, 339–346, <https://doi.org/10.1038/ngeo1797>, 2013.

992 PAGES Hydro2k Consortium: Comparing proxy and model estimates of hydroclimate variability  
993 and change over the Common Era, *Climate of the Past*, 13, 1851–1900,  
994 <https://doi.org/10.5194/cp-13-1851-2017>, 2017.

995 PAGES2k Consortium, Emile-Geay, J., McKay, N. P., Kaufman, D. S., Gunten, L. von, Wang, J.,  
996 Anchukaitis, K. J., Abram, N. J., Addison, J. A., Curran, M. A. J., Evans, M. N., Henley, B. J., Hao,  
997 Z., Martrat, B., McGregor, H. V., Neukom, R., Pederson, G. T., Stenni, B., Thirumalai, K.,  
998 Werner, J. P., Xu, C., Divine, D. V., Dixon, B. C., Gergis, J., Mundo, I. A., Nakatsuka, T., Phipps, S.  
999 J., Routson, C. C., Steig, E. J., Tierney, J. E., Tyler, J. J., Allen, K. J., Bertler, N. A. N., Björklund, J.,

- 1000 Chase, B. M., Chen, M.-T., Cook, E., Jong, R. de, DeLong, K. L., Dixon, D. A., Ekaykin, A. A., Ersek,  
1001 V., Filipsson, H. L., Francus, P., Freund, M. B., Frezzotti, M., Gaire, N. P., Gajewski, K., Ge, Q.,  
1002 Goosse, H., Gornostaeva, A., Grosjean, M., Horiuchi, K., Hormes, A., Husum, K., Isaksson, E.,  
1003 Kandasamy, S., Kawamura, K., Kilbourne, K. H., Koç, N., Leduc, G., Linderholm, H. W., Lorrey, A.  
1004 M., Mikhalenko, V., Mortyn, P. G., Motoyama, H., Moy, A. D., Mulvaney, R., Munz, P. M., Nash,  
1005 D. J., Oerter, H., Opel, T., Orsi, A. J., Ovchinnikov, D. V., Porter, T. J., Roop, H. A., Saenger, C.,  
1006 Sano, M., Sauchyn, D., Saunders, K. M., Seidenkrantz, M.-S., Severi, M., Shao, X., Sicre, M.-A.,  
1007 Sigl, M., Sinclair, K., George, S. S., Jacques, J.-M. S., Thamban, M., Thapa, U. K., Thomas, E. R.,  
1008 Turney, C., Uemura, R., Viau, A. E., Vladimirova, D. O., Wahl, E. R., White, J. W. C., Yu, Z., and  
1009 Zinke, J.: A global multiproxy database for temperature reconstructions of the Common Era,  
1010 *Scientific Data*, 4, sdata201788, <https://doi.org/10.1038/sdata.2017.88>, 2017.
- 1011 Peregrine, P. N.: Climate and social change at the start of the Late Antique Little Ice Age, *The*  
1012 *Holocene*, 30, 1643–1648, <https://doi.org/10.1177/0959683620941079>, 2020.
- 1013 Pérez-Mejías, C., Moreno, A., Sancho, C., Bartolomé, M., Stoll, H., Osácar, M. C., Cacho, I., and  
1014 Delgado-Huertas, A.: Transference of isotopic signal from rainfall to dripwaters and farmed  
1015 calcite in Mediterranean semi-arid karst, *Geochimica et Cosmochimica Acta*, 243, 66–98,  
1016 <https://doi.org/10.1016/j.gca.2018.09.014>, 2018.
- 1017 Pérez-Zanón, N., Sigró, J., and Ashcroft, L.: Temperature and precipitation regional climate  
1018 series over the central Pyrenees during 1910–2013, *International Journal of Climatology*, 37,  
1019 1922–1937, <https://doi.org/10.1002/joc.4823>, 2017.
- 1020 Pla, S. and Catalan, J.: Chrysophyte cysts from lake sediments reveal the submillennial  
1021 winter/spring climate variability in the northwestern Mediterranean region throughout the  
1022 Holocene, *Climate Dynamics*, 24, 263–278, <https://doi.org/10.1007/s00382-004-0482-1>, 2005.
- 1023 Pla-Rabes, S. and Catalan, J.: Deciphering chrysophyte responses to climate seasonality, *J*  
1024 *Paleolimnol*, 46, 139, <https://doi.org/10.1007/s10933-011-9529-6>, 2011.
- 1025 Priestley, S. C., Treble, P. C., Griffiths, A. D., Baker, A., Abram, N. J., and Meredith, K. T.: Caves  
1026 demonstrate decrease in rainfall recharge of southwest Australian groundwater is  
1027 unprecedented for the last 800 years, *Commun Earth Environ*, 4, 1–12,  
1028 <https://doi.org/10.1038/s43247-023-00858-7>, 2023.
- 1029 Reimer, P.: Discussion: Reporting and Calibration of Post-Bomb 14C Data, *Radiocarbon*, 46,  
1030 1299–1304, <https://doi.org/10.1017/S0033822200033154>, 2004.
- 1031 Rico, I., Izagirre, E., Serrano, E., and López-Moreno, J. I.: Superficie glaciar actual en los  
1032 Pirineos: Una actualización para 2016, *Pirineos*, 172, 029,  
1033 <https://doi.org/10.3989/Pirineos.2017.172004>, 2017.
- 1034 Sánchez-López, G., Hernández, A., Pla-Rabes, S., Trigo, R. M., Toro, M., Granados, I., Sáez, A.,  
1035 Masqué, P., Pueyo, J. J., Rubio-Inglés, M. J., and Giral, S.: Climate reconstruction for the last  
1036 two millennia in central Iberia: The role of East Atlantic (EA), North Atlantic Oscillation (NAO)  
1037 and their interplay over the Iberian Peninsula, *Quaternary Science Reviews*, 149, 135–150,  
1038 <https://doi.org/10.1016/j.quascirev.2016.07.021>, 2016.
- 1039 Sancho, C., Belmonte, Á., Bartolomé, M., Moreno, A., Leunda, M., and López-Martínez, J.:  
1040 Middle-to-late Holocene palaeoenvironmental reconstruction from the A294 ice-cave record  
1041 (Central Pyrenees, northern Spain), *Earth and Planetary Science Letters*, 484, 135–144,  
1042 <https://doi.org/10.1016/j.epsl.2017.12.027>, 2018.

- 1043 Scholz, D. and Hoffmann, D. L.: StalAge - An algorithm designed for construction of speleothem  
1044 age models, *Quaternary Geochronology*, 6, 369–382,  
1045 <https://doi.org/10.1016/j.quageo.2011.02.002>, 2011.
- 1046 Schurer, A. P., Tett, S. F. B., and Hegerl, G. C.: Small influence of solar variability on climate  
1047 over the past millennium, *Nature Geosci*, 7, 104–108, <https://doi.org/10.1038/ngeo2040>,  
1048 2014.
- 1049 Shen, C. C., Edwards, R. L., Cheng, H., Dorale, J. A., Thomas, R. B., Moran, S. B., Weinstein, S. E.,  
1050 and Edmonds, H. N.: Uranium and thorium isotopic and concentration measurements by  
1051 magnetic sector inductively coupled plasma mass spectrometry, *Chemical Geology*, 185, 165–  
1052 178, 2002.
- 1053 Shindell, D. T., Schmidt, G. A., Mann, M. E., Rind, D., and Waple, A.: benito, *Science*, 294, 2149,  
1054 2001.
- 1055 Sigl, M., Winstrup, M., McConnell, J. R., Welten, K. C., Plunkett, G., Ludlow, F., Büntgen, U.,  
1056 Caffee, M., Chellman, N., Dahl-Jensen, D., Fischer, H., Kipfstuhl, S., Kostick, C., Maselli, O. J.,  
1057 Mekhaldi, F., Mulvaney, R., Muscheler, R., Pasteris, D. R., Pilcher, J. R., Salzer, M., Schüpbach,  
1058 S., Steffensen, J. P., Vinther, B. M., and Woodruff, T. E.: Timing and climate forcing of volcanic  
1059 eruptions for the past 2,500 years, *Nature*, 523, 543–549,  
1060 <https://doi.org/10.1038/nature14565>, 2015.
- 1061 Spötl, C.: Long-term performance of the Gasbench isotope ratio mass spectrometry system for  
1062 the stable isotope analysis of carbonate microsamples, *Rapid Commun. Mass Spectrom.*, 25,  
1063 1683–1685, <https://doi.org/10.1002/rcm.5037>, 2011.
- 1064 Steffen, W., Broadgate, W., Deutsch, L., Gaffney, O., and Ludwig, C.: The trajectory of the  
1065 Anthropocene: The Great Acceleration, *The Anthropocene Review*, 2, 81–98,  
1066 <https://doi.org/10.1177/2053019614564785>, 2015.
- 1067 Sundqvist, H. S., Holmgren, K., Moberg, A., Spötl, C., and Mangini, A.: Stable isotopes in a  
1068 stalagmite from NW Sweden document environmental changes over the past 4000 years,  
1069 *Boreas*, 39, 77–86, <https://doi.org/10.1111/j.1502-3885.2009.00099.x>, 2010.
- 1070 Swingedouw, D., Terray, L., Cassou, C., Voldoire, A., Salas-Melia, D., and Servonnat, J.: Natural  
1071 forcing of climate during the last millennium: fingerprint of solar variability, *Climate Dynamics*,  
1072 36, 1349–1364, <https://doi.org/10.1007/s00382-010-0803-5>, 2011.
- 1073 Tadros, C. V., Markowska, M., Treble, P. C., Baker, A., Frisia, S., Adler, L., and Drysdale, R. N.:  
1074 Recharge variability in Australia’s southeast alpine region derived from cave monitoring and  
1075 modern stalagmite  $\delta^{18}\text{O}$  records, *Quaternary Science Reviews*, 295, 107742,  
1076 <https://doi.org/10.1016/j.quascirev.2022.107742>, 2022.
- 1077 Thatcher, D. L., Wanamaker, A. D., Denniston, R. F., Ummenhofer, C. C., Asmerom, Y., Polyak,  
1078 V. J., Cresswell-Clay, N., Hasiuk, F., Haws, J., and Gillikin, D. P.: Iberian hydroclimate variability  
1079 and the Azores High during the last 1200 years: evidence from proxy records and climate  
1080 model simulations, *Clim Dyn*, <https://doi.org/10.1007/s00382-022-06427-6>, 2022.
- 1081 Trachsel, M., Kamenik, C., Grosjean, M., McCarroll, D., Moberg, A., Brázdil, R., Büntgen, U.,  
1082 Dobrovolný, P., Esper, J., Frank, D. C., Friedrich, M., Glaser, R., Larocque-Tobler, I., Nicolussi, K.,  
1083 and Riemann, D.: Multi-archive summer temperature reconstruction for the European Alps,

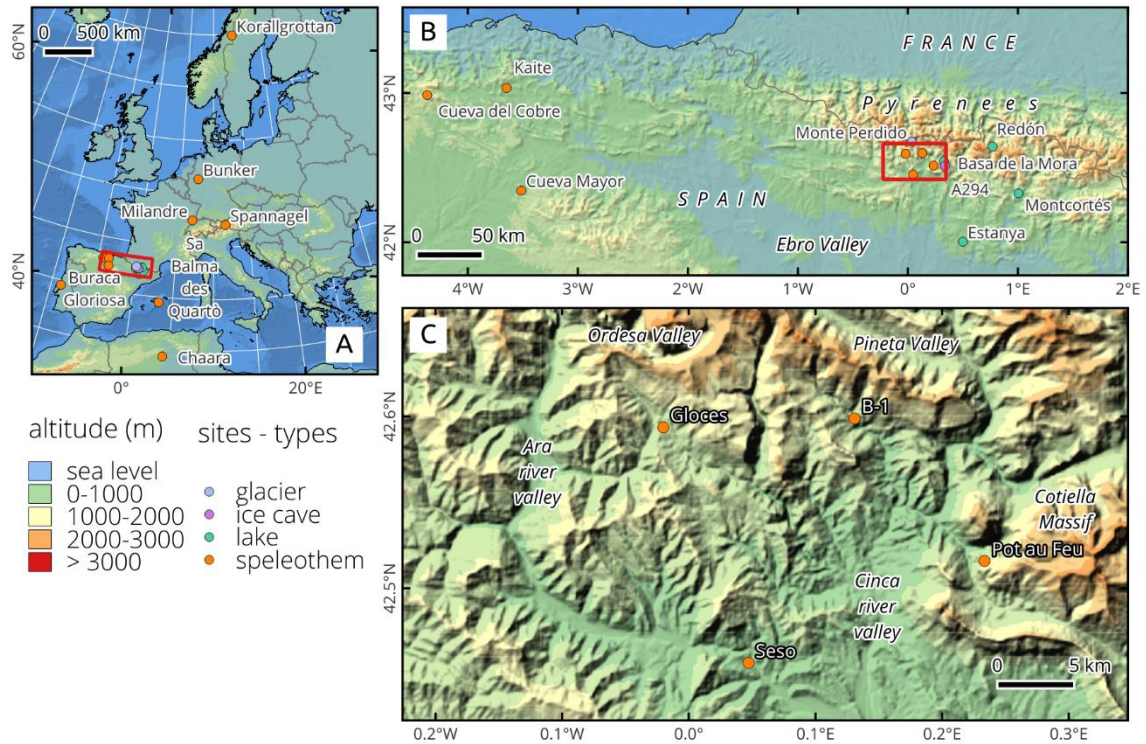


- 1084 AD 1053–1996, *Quaternary Science Reviews*, 46, 66–79,  
1085 <https://doi.org/10.1016/j.quascirev.2012.04.021>, 2012.
- 1086 Treble, P. C., Baker, A., Abram, N. J., Hellstrom, J. C., Crawford, J., Gagan, M. K., Borsato, A.,  
1087 Griffiths, A. D., Bajo, P., Markowska, M., Priestley, S. C., Hankin, S., and Paterson, D.:  
1088 Ubiquitous karst hydrological control on speleothem oxygen isotope variability in a global  
1089 study, *Commun Earth Environ*, 3, 1–10, <https://doi.org/10.1038/s43247-022-00347-3>, 2022.
- 1090 Tremaine, D. M., Froelich, P. N., and Wang, Y.: Speleothem calcite farmed in situ: Modern  
1091 calibration of  $\delta^{18}\text{O}$  and  $\delta^{13}\text{C}$  paleoclimate proxies in a continuously-monitored natural cave  
1092 system, *Geochimica et Cosmochimica Acta*, 75, 4929–4950,  
1093 <https://doi.org/10.1016/j.gca.2011.06.005>, 2011.
- 1094 Trouet, V., Esper, J., Graham, N. E., Baker, A., Scourse, J. D., and Frank, D. C.: Persistent Positive  
1095 North Atlantic Oscillation Mode Dominated the Medieval Climate Anomaly, *Science*, 324, 78–  
1096 80, 2009.
- 1097 Trouet, V., Scourse, J. D., and Raible, C. C.: North Atlantic storminess and Atlantic Meridional  
1098 Overturning Circulation during the last Millennium: Reconciling contradictory proxy records of  
1099 NAO variability, *Global and Planetary Change*, 84–85, 48–55,  
1100 <https://doi.org/10.1016/j.gloplacha.2011.10.003>, 2012.
- 1101 Usoskin, I. G., Hulot, G., Gallet, Y., Roth, R., Licht, A., Joos, F., Kovaltsov, G. A., Thébault, E., and  
1102 Khokhlov, A.: Evidence for distinct modes of solar activity, *A&A*, 562, L10,  
1103 <https://doi.org/10.1051/0004-6361/201423391>, 2014.
- 1104 Usoskin, I. G., Gallet, Y., Lopes, F., Kovaltsov, G. A., and Hulot, G.: Solar activity during the  
1105 Holocene: the Hallstatt cycle and its consequence for grand minima and maxima, *A&A*, 587,  
1106 A150, <https://doi.org/10.1051/0004-6361/201527295>, 2016.
- 1107 Vegas-Vilarrúbia, T., Corella, J. P., Sigró, J., Rull, V., Dorado-Liñan, I., Valero-Garcés, B., and  
1108 Gutiérrez-Merino, E.: Regional precipitation trends since 1500 CE reconstructed from calcite  
1109 sublayers of a varved Mediterranean lake record (Central Pyrenees), *Science of The Total  
1110 Environment*, 826, 153773, <https://doi.org/10.1016/j.scitotenv.2022.153773>, 2022.
- 1111 Vicente de Vera García, A., Mata-Campo, M. P., Pla, S., Vicente, E., Prego, R., Frugone-Álvarez,  
1112 M., Polanco-Martínez, J., Galofré, M., and Valero-Garcés, B. L.: Unprecedented recent regional  
1113 increase in organic carbon and lithogenic fluxes in high altitude Pyrenean lakes, *Sci Rep*, 13,  
1114 8586, <https://doi.org/10.1038/s41598-023-35233-1>, 2023.
- 1115 Vidaller, I., Revuelto, J., Izagirre, E., Rojas-Heredia, F., Alonso-González, E., Gascoin, S., René, P.,  
1116 Berthier, E., Rico, I., Moreno, A., Serrano, E., Serreta, A., and López-Moreno, J. I.: Toward an  
1117 Ice-Free Mountain Range: Demise of Pyrenean Glaciers During 2011–2020, *Geophys Res Lett*,  
1118 48, <https://doi.org/10.1029/2021GL094339>, 2021.
- 1119 Welte, C., Wacker, L., Hattendorf, B., Christl, M., Koch, J., Synal, H.-A., and Günther, D.: Novel  
1120 Laser Ablation Sampling Device for the Rapid Radiocarbon Analysis of Carbonate Samples by  
1121 Accelerator Mass Spectrometry, *Radiocarbon*, 58, 419–435,  
1122 <https://doi.org/10.1017/RDC.2016.6>, 2016.
- 1123 Zawiska, I., Luoto, T. P., Nevalainen, L., Tylmann, W., Jensen, T. C., Obremaska, M., Słowiński,  
1124 M., Woszczyk, M., Schartau, A. K., and Walseng, B.: Climate variability and lake ecosystem  
1125 responses in western Scandinavia (Norway) during the last Millennium, *Palaeogeography*,

1126 Palaeoclimatology, Palaeoecology, 466, 231–239,  
1127 <https://doi.org/10.1016/j.palaeo.2016.11.034>, 2017.  
1128

1129 **Figure captions**

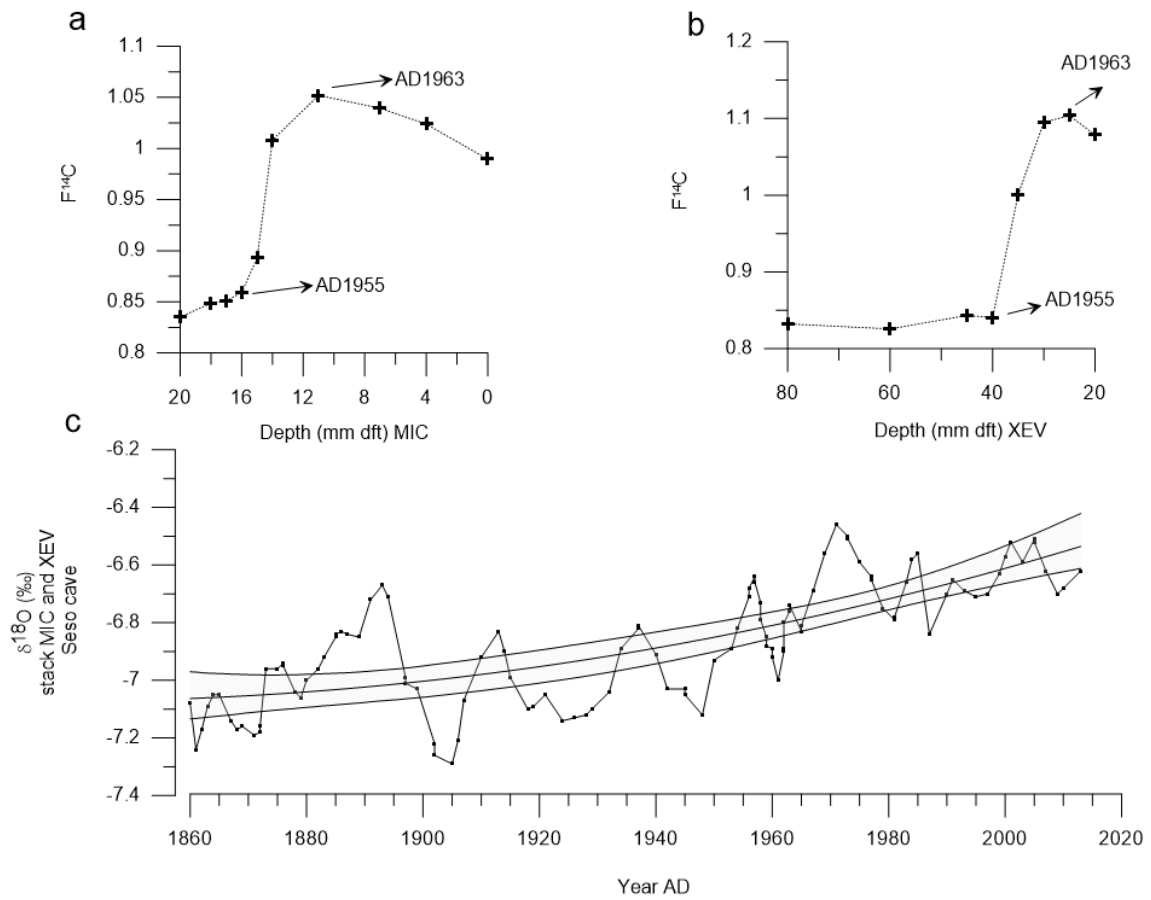
1130 **Figure 1.** a) Location of regional speleothem records covering last 2500 years to be compared with the  
 1131 samples studied in the Pyrenees (red rectangle, enlarged in Fig. 1B). b) Location of caves (orange circles)  
 1132 and other nearby records from northern Spain. See legend for the different types of available paleoclimate  
 1133 archives. c) Location of the four studied caves in the Central Pyrenees of NE Spain in the vicinity of the  
 1134 Ordesa and Monte Perdido National Park. Source base map: digital elevation model and hillshade derived  
 1135 from Mapzen Global Terrain, coastline, boundaries and geographic lines from NaturalEarthData.com



1136

1137

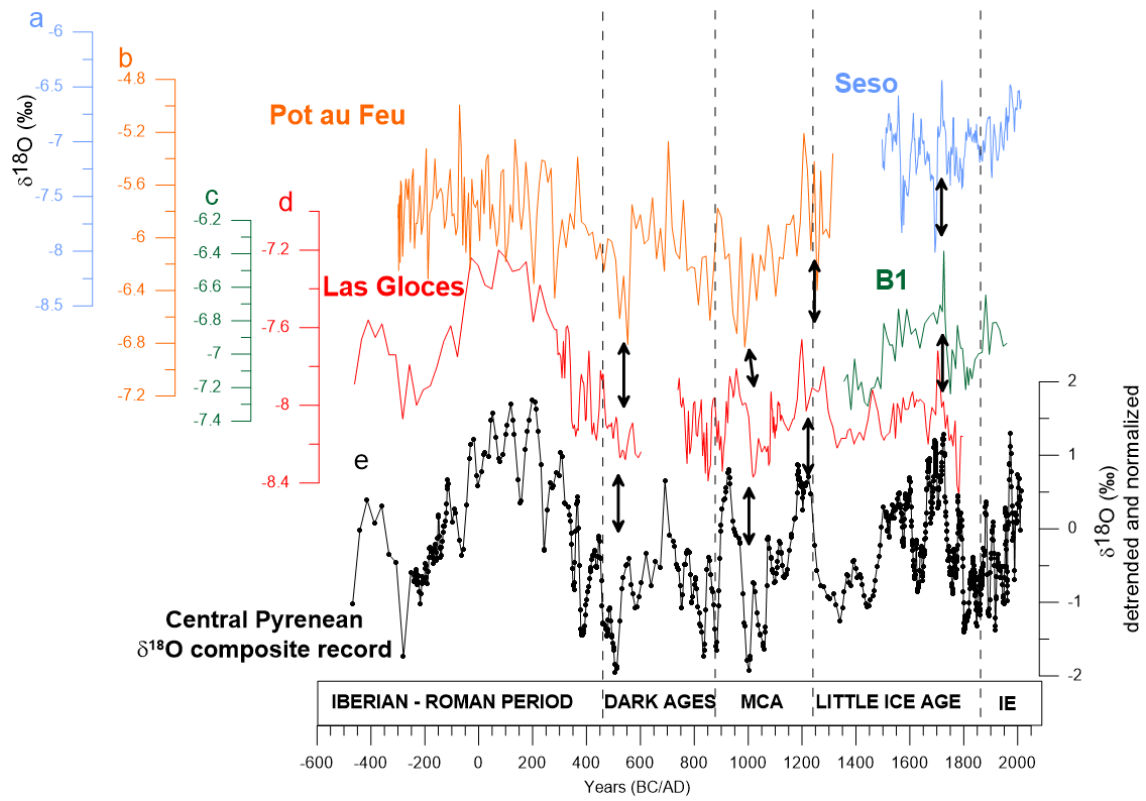
1138 **Figure 2.**  $^{14}\text{C}$  activity (expressed as  $F^{14}\text{C}$ , following recommendations made in Reimer, 2004) of the top  
1139 parts of stalagmites MIC (a) and XEV (b) from Seso Cave. The start of the increase in  $F^{14}\text{C}$  and its  
1140 maximum are recorded at 1955 and 1963 CE, respectively, in both stalagmites. c) Composite  $\delta^{18}\text{O}$  record  
1141 using *Iscam* with data from MIC and XEV stalagmites.



1142

1143

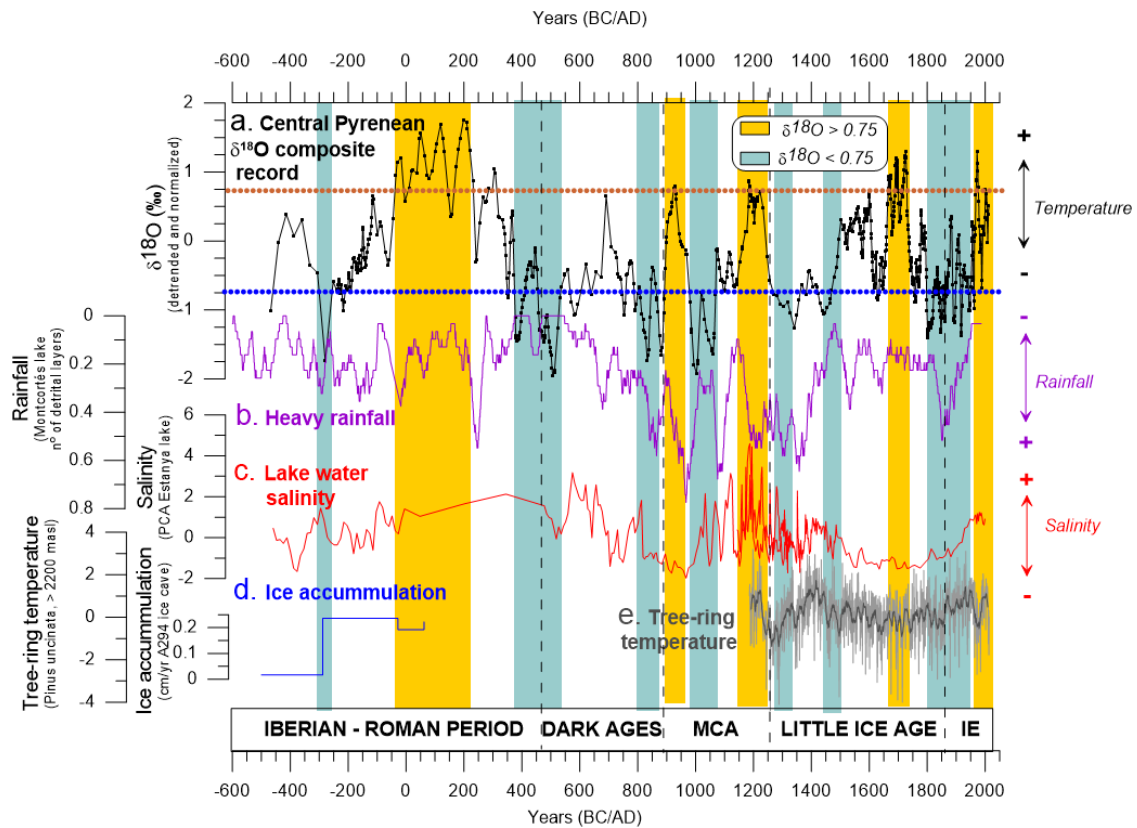
1144 **Figure 3.** Comparison of individual  $\delta^{18}\text{O}$  records from four Pyrenean caves, (a) Seso; (b) Pot au Feu; (c)  
 1145 B1 and (d) Las Gloces caves, and (e) the composite  $\delta^{18}\text{O}$  record produced using *Iscam* (black curve) for the  
 1146 last 2500 years. Generating Seso and Las Gloces curves required *Iscam* age modelling while Pot au Feu  
 1147 and B1 curves represent only one stalagmite, which age model was produced by *StalAge* modelling. Black  
 1148 double arrows indicate intervals with patterns present in all records. MCA: Medieval Climate Anomaly,  
 1149 IE: Industrial Era.



1150

1151

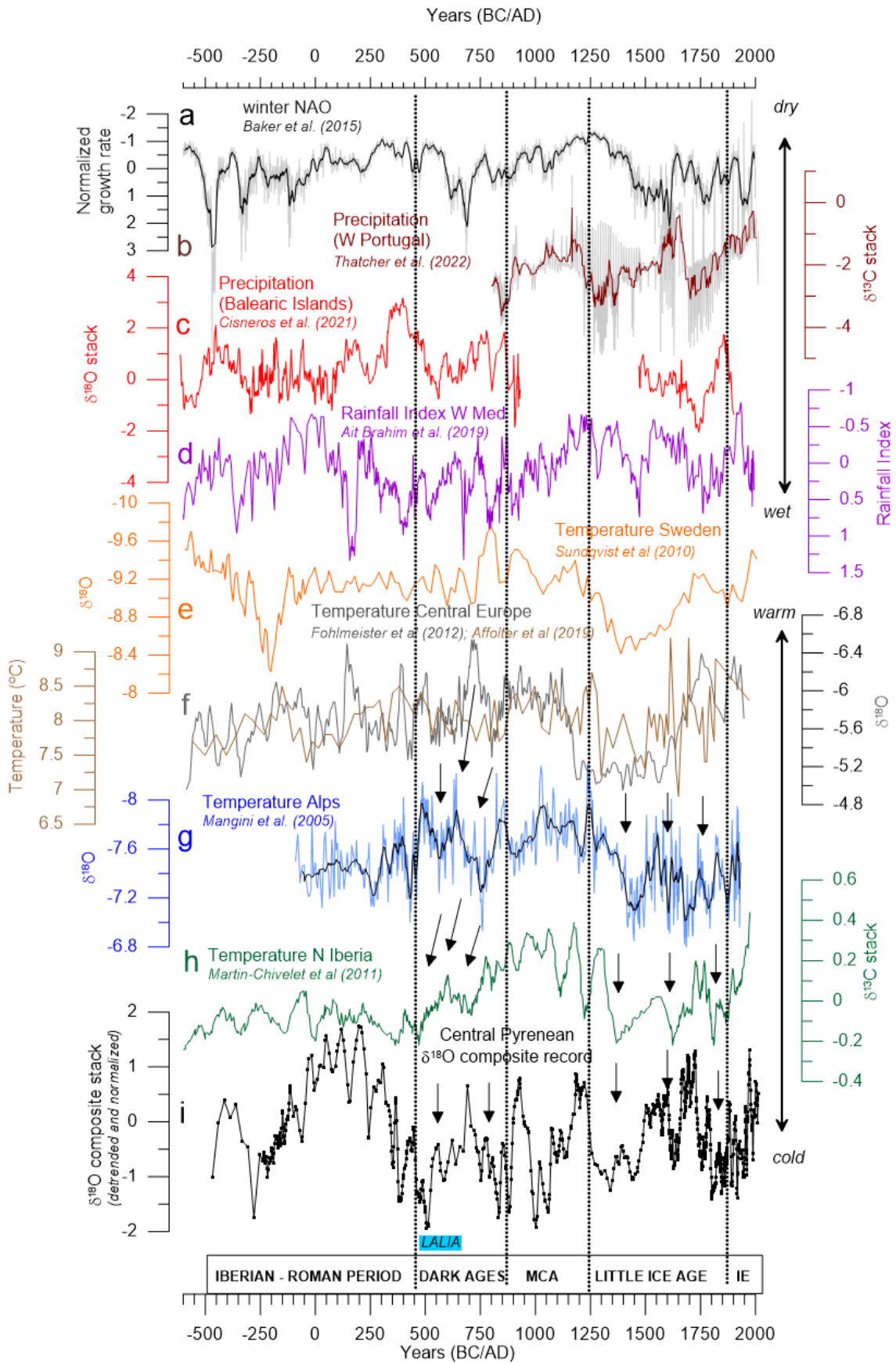
1152 **Figure 4.** a) Central Pyrenean  $\delta^{18}\text{O}$  composite record for the last 2500 years based on eight stalagmites  
 1153 from four caves. Blue bars mark intervals of  $\delta^{18}\text{O}$  values below  $-0.75$ , while yellow bars mark those with  
 1154  $\delta^{18}\text{O}$  values above  $+0.75$  (note this composite record was obtained from normalized records, so it varies  
 1155 among  $-3$  and  $3$  without possibility of direct translation to absolute  $\delta^{18}\text{O}$  values). b) Rainfall reconstructed  
 1156 from calcite layers from Montcortés lake in the Pre-Pyrenees (Corella et al., 2016). c) Salinity reconstructed  
 1157 from geochemical data from Estanya lake in the Pre-Pyrenees (González-Sampéris et al., 2017; Morellón  
 1158 et al., 2012, 2011). d) Snow and ice accumulation in ice cave A294 in the Cotiella massif of the Central  
 1159 Pyrenees (Sancho et al., 2018), and e) Pyrenean temperature reconstruction based on tree-ring data  
 1160 (Büntgen et al., 2017). MCA: Medieval Climate Anomaly, IE: Industrial Era.



1161

1162

1163 **Figure 5.** Comparison of European and W Mediterranean speleothem records covering the last 2500 years.  
1164 a) winter NAO reconstruction based on growth rate of Irish speleothems (Baker et al., 2015); b)  
1165 precipitation variability reconstructed for W Portugal (Thatcher et al., 2022), c) Balearic Islands (Cisneros  
1166 et al., 2021), and d) Morocco (Ait Brahim et al., 2019); temperature variation reconstructed from e) Sweden  
1167 (Sundqvist et al., 2010), f) Central Europe (Affolter et al., 2019; Fohlmeister et al., 2012), g) Alps (Mangini  
1168 et al., 2005) and h) Northern Iberia (Martín-Chivelet et al., 2011); i) Central Pyrenean  $\delta^{18}\text{O}$  composite  
1169 record (this study). Black arrows indicate intervals of well-reproduced patterns during the Dark Ages and  
1170 the Little Ice Age cold intervals. MCA: Medieval Climate Anomaly, IE: Industrial Era.

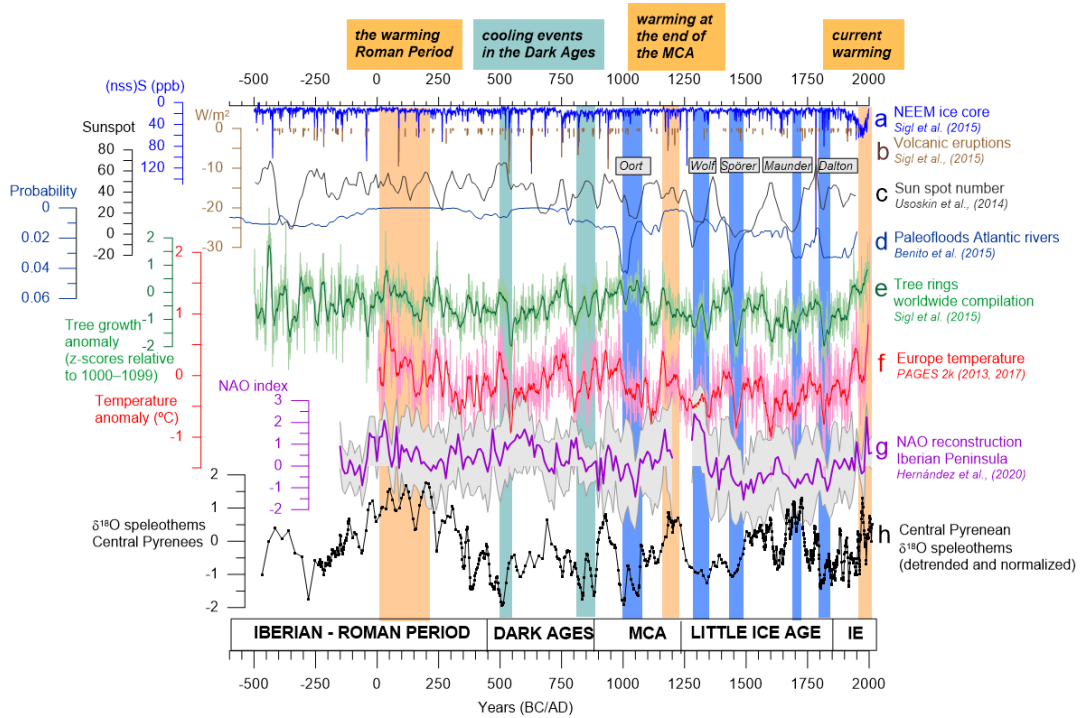


1171

1172



1173 **Figure 6.** Global records and forcing mechanisms. a) volcanic forcing represented by the (nss)S (ppb) in  
 1174 the NEEM ice core (blue line); b) changes in the irradiance as a consequence of Northern Hemisphere  
 1175 volcanic eruptions (Sigl et al., 2015) (brown bars); c) sunspot numbers (Usoskin et al., 2014); d) probability  
 1176 of paleofloods in European temperate regions (Benito et al., 2015); e) worldwide tree-ring compilation  
 1177 (green line, running average width window = 15) (Sigl et al., 2015); f) temperature reconstruction from  
 1178 Europe, compiled by the PAGES2k group (red line, running average width window = 15) (PAGES 2k  
 1179 Consortium, 2013); g) the NAO reconstruction for the Central Iberian Peninsula (purple line) and the 95%  
 1180 (light grey band) uncertainty intervals and h) Central Pyrenean  $\delta^{18}\text{O}$  composite record (this study). Light  
 1181 brown bars indicate warming periods during the Roman Period, the end of the MCA and in recent decades.  
 1182 Light blue bands mark cooling events during the DA while dark blue bands mark solar minima (Oort, Wolf,  
 1183 Spörer, Maunder and Dalton).



1184

1185

1186 **Table 1.** Sample characteristics

| <b>Cave</b>       | <b>Sample ID</b> | <b>Length (cm)</b>         | <b>Number of U-Th dates (used in StalAge)</b> | <b>Interval covered (years BCE/CE in StalAge)</b> | <b>Sampling resolution (average years per isotope sample)</b> | <b>Comments</b>  |
|-------------------|------------------|----------------------------|---|---|---|--|
| <i>Seso</i>       | MIC              | 8.5                        | 8   | 1718-2010 CE                                      | 3.8 years   | Growth to present                                      |
|                   | XEV              | 26                         | 9   | 1501-2013 CE                                      | 1.9 years   | Two growth periods, no hiatus. Growth to present       |
|                   | CHA              | 8.5                        | 3   | 1573-1779 CE                                      | 3.5 years   | The uppermost 7 mm are not sampled                     |
|                   | CLA              | 10.5 (a hiatus at 8.5 cm)  | 4   | 1826-1935 CE                                      | 1.5 years   | The uppermost 2 cm are not sampled                     |
| <i>Las Gloces</i> | ISA              | 13.5 (a hiatus at 7 cm)    | 7   | 346-607 CE<br>845-634 CE                          | 11.4 years  | In StalAge, one date is not included due to high error |
|                   | LUC              | 23.3 (a hiatus at 12.5 cm) | 6   | 471BCE-504 CE<br>547-1991 CE                      | 11.2 years  | Really short hiatus                                    |
| <i>B-1</i>        | TAR              | 7.5 cm                     | 8   | 1355-1959 CE                                      | 10.5 years  |  |
| <i>Pot au Feu</i> | JAR              | 80 cm                      | 10  | 299BCE-1314 CE                                    | 10 years  |  |

1187

1188

1189  
1190  
1191  
1192  
1193

**Table 2.**  $^{230}\text{Th}$  dating results of the eight stalagmites examined in this study (data from the University of Minnesota, University of Xi'an and University of Melbourne). Analytical errors are  $2\sigma$  of the mean. The sample marked by a red asterisk was discarded due to the high error.

| Sample ID              | $^{230}\text{Th}$ (ppb) | $^{232}\text{Th}$ (ppb) | $^{230}\text{Th}/^{232}\text{Th}$ (b) | $\delta^{230}\text{Th}$ (‰) (measured) | $^{230}\text{Th}/^{238}\text{U}$ (a) | $^{230}\text{Th}$ Age (yr) (uncorrected) | $^{230}\text{Th}$ Age (yr) (corrected) | $\delta^{230}\text{Th}_{\text{true}}$ (‰) (corrected) | $^{230}\text{Th}$ Age (yr BP) (corrected) |
|------------------------|-------------------------|-------------------------|---------------------------------------|--|--------------------------------------|--|--|---|---|
| <b>Seso Cave</b>       |                         |                         |                                       |  |                                      |  |  |   |   |
| Xer-0                  | 451 ±1                  | 12292 ±248              | 4.0 ±0.1                              | 434.3 ±3.1                             | 0.006 ±0.001                         | 495 ±8                                   | -52 ±87                                | 454 ±3  | 115 ±387                                  |
| Xer-5                  | 335 ±1                  | 2875 ±58                | 4.2 ±0.2                              | 434.3 ±2.9                             | 0.0021 ±0.0001                       | 159 ±8                                   | -6 ±116                                | 434 ±3  | -69 ±116                                  |
| Xer-8S                 | 299 ±1                  | 1557 ±31                | 8 ±0                                  | 424.6 ±3.1                             | 0.0027 ±0.0001                       | 204 ±9                                   | 97 ±76                                 | 425 ±3  | 34 ±76                                    |
| Xer-110                | 308 ±1                  | 798 ±16                 | 18 ±1                                 | 410.5 ±2.4                             | 0.0029 ±0.0001                       | 223 ±9                                   | 170 ±39                                | 411 ±2  | 107 ±39                                   |
| Xer-14S                | 267 ±1                  | 535 ±11                 | 25 ±1                                 | 404.7 ±2.7                             | 0.0030 ±0.0001                       | 256 ±10                                  | 195 ±31                                | 405 ±3  | 132 ±31                                   |
| Xer-190                | 261 ±1                  | 340 ±7                  | 54 ±2                                 | 419.0 ±2.8                             | 0.0033 ±0.0001                       | 328 ±10                                  | 301 ±22                                | 419 ±3  | 238 ±22                                   |
| Xer-210                | 299 ±1                  | 1445 ±29                | 20 ±1                                 | 420.8 ±3.5                             | 0.0039 ±0.0002                       | 452 ±12                                  | 353 ±71                                | 421 ±4  | 290 ±71                                   |
| Xer-240                | 277 ±1                  | 1758 ±35                | 19 ±1                                 | 436.4 ±2.7                             | 0.0072 ±0.0002                       | 548 ±12                                  | 420 ±92                                | 437 ±3  | 357 ±92                                   |
| Xer-280                | 339 ±1                  | 2459 ±50                | 20 ±0                                 | 414.7 ±2.8                             | 0.0086 ±0.0001                       | 667 ±10                                  | 517 ±106                               | 415 ±4  | 454 ±106                                  |
| Mic-0                  | 503 ±1                  | 4623 ±93                | 5 ±0                                  | 485.9 ±2.4                             | 0.0027 ±0.0001                       | 196 ±6                                   | 16 ±128                                | 486 ±2  | -46 ±128                                  |
| Mic-5                  | 441 ±1                  | 1166 ±23                | 6 ±1                                  | 487.3 ±2.3                             | 0.0039 ±0.0002                       | 69 ±11                                   | 17 ±38                                 | 487 ±2  | -45 ±38                                   |
| Mic-20                 | 412 ±1                  | 127 ±3                  | 7.3 ±6                                | 477.0 ±2.3                             | 0.0014 ±0.0001                       | 101 ±8                                   | 95 ±9                                  | 477 ±2  | 33 ±9                                     |
| Mic-35                 | 427 ±1                  | 708 ±14                 | 2.5 ±1                                | 455.2 ±2.3                             | 0.0030 ±0.0001                       | 191 ±8                                   | 158 ±25                                | 455 ±2  | 96 ±25                                    |
| Mic-48                 | 417 ±1                  | 603 ±12                 | 3.4 ±1                                | 457.7 ±3.0                             | 0.0030 ±0.0001                       | 223 ±8                                   | 205 ±15                                | 456 ±3  | 142 ±15                                   |
| Mic-60                 | 393 ±1                  | 1049 ±21                | 2.3 ±1                                | 461.4 ±3.8                             | 0.0037 ±0.0001                       | 274 ±8                                   | 242 ±24                                | 462 ±4  | 179 ±24                                   |
| Mic-67                 | 413 ±1                  | 3812 ±77                | 9 ±0                                  | 458.7 ±2.9                             | 0.0031 ±0.0001                       | 380 ±8                                   | 196 ±30                                | 459 ±3  | 134 ±30                                   |
| Mic-75                 | 389 ±1                  | 25715 ±517              | 4 ±0                                  | 458.0 ±2.5                             | 0.014 ±0.0002                        | 1080 ±15                                 | 267 ±576                               | 458 ±3  | 204 ±576                                  |
| Cha-0                  | 346 ±1                  | 332 ±7                  | 3.4 ±2                                | 371.5 ±3.1                             | 0.0020 ±0.0001                       | 158 ±9                                   | 138 ±17                                | 372 ±3  | 75 ±17                                    |
| Cha-2S                 | 368 ±1                  | 493 ±10                 | 3.2 ±1                                | 367.1 ±2.9                             | 0.0026 ±0.0001                       | 204 ±8                                   | 176 ±22                                | 367 ±3  | 113 ±22                                   |
| Cha-70                 | 346 ±1                  | 1262 ±25                | 17 ±1                                 | 367.8 ±2.4                             | 0.0030 ±0.0001                       | 298 ±8                                   | 221 ±56                                | 368 ±2  | 158 ±56                                   |
| Cha-74                 | 319 ±1                  | 226 ±5                  | 7.0 ±3                                | 368.6 ±2.7                             | 0.0030 ±0.0001                       | 240 ±9                                   | 225 ±14                                | 369 ±3  | 162 ±14                                   |
| Cha-0                  | 393.0 ±0.7              | 169 ±3                  | 11.6 ±6                               | 381.0 ±2.0                             | 0.0030 ±0.0001                       | 239 ±11                                  | 230 ±13                                | 381 ±2  | 168 ±13                                   |
| Cha-30                 | 342.9 ±1.0              | 609 ±12                 | 47 ±2                                 | 381.2 ±3.0                             | 0.0030 ±0.0001                       | 398 ±12                                  | 360 ±29                                | 382 ±3  | 298 ±29                                   |
| Cha-58                 | 348.1 ±0.8              | 396 ±8                  | 84 ±2                                 | 387.3 ±2.7                             | 0.0038 ±0.0001                       | 457 ±9                                   | 434 ±19                                | 388 ±3  | 372 ±19                                   |
| <b>Las Cloves cave</b> |                         |                         |                                       |  |                                      |  |  |   |   |
| Isa-0                  | 167.1 ±0.3              | 451 ±9                  | 233 ±5                                | 1465.3 ±3.4                            | 0.0382 ±0.0003                       | 1700 ±14                                 | 1668 ±26                               | 1472 ±3   | 1605 ±26                                  |
| Isa-4                  | 119.9 ±0.2              | 291 ±6                  | 221 ±5                                | 1487.0 ±4.1                            | 0.0235 ±0.0003                       | 1454 ±15                                 | 1406 ±25                               | 1493 ±4   | 1343 ±25                                  |
| Isa-4S                 | 115.0 ±0.1              | 905 ±18                 | 61 ±2                                 | 1510.8 ±1.9                            | 0.0289 ±0.0004                       | 1262 ±19                                 | 1171 ±67                               | 1516 ±3   | 1108 ±67                                  |
| Isa-6                  | 107.7 ±0.2              | 832 ±171                | 5 ±1                                  | 1504.8 ±4.5                            | 0.0233 ±0.0004                       | 1107 ±20                                 | 185 ±63                                | 1506 ±5   | 122 ±63                                   |
| Isa-8                  | 108.4 ±0.1              | 261 ±5                  | 142 ±4                                | 1504.6 ±3.6                            | 0.0207 ±0.0004                       | 905 ±17                                  | 877 ±26                                | 1508 ±5   | 814 ±26                                   |
| Isa-11                 | 69.5 ±0.1               | 2977 ±60                | 8 ±1                                  | 1505.3 ±3.7                            | 0.0201 ±0.0006                       | 877 ±26                                  | 379 ±353                               | 1507 ±4   | 316 ±353                                  |
| Luc-0                  | 113 ±1                  | 2350 ±47                | 5.7 ±1                                | 1859 ±4                                | 0.0649 ±0.0006                       | 2693 ±23                                 | 2483 ±150                              | 1872 ±4   | 2420 ±150                                 |
| Luc-5.5                | 88 ±1                   | 539 ±11                 | 127 ±3                                | 1848 ±4                                | 0.0649 ±0.0006                       | 1806 ±18                                 | 1744 ±47                               | 1857 ±4   | 1681 ±47                                  |
| Luc-10                 | 131 ±0.2                | 388 ±8                  | 213 ±5                                | 1721.6 ±3.2                            | 0.0382 ±0.0003                       | 1540 ±16                                 | 1508 ±27                               | 1729 ±3.2   | 1445 ±27                                  |
| Luc-11                 | 81 ±1                   | 955 ±19                 | 50 ±1                                 | 1796 ±5                                | 0.0359 ±0.0006                       | 1407 ±23                                 | 1284 ±90                               | 1803 ±5   | 1221 ±90                                  |
| Luc-15.5               | 73 ±0                   | 282 ±6                  | 118 ±3                                | 1783 ±6                                | 0.0279 ±0.0006                       | 1098 ±22                                 | 1057 ±36                               | 1789 ±6   | 994 ±36                                   |
| Luc-18.5               | 72 ±0                   | 1477 ±30                | 1.6 ±1                                | 1705 ±5                                | 0.0202 ±0.0005                       | 818 ±22                                  | 597 ±158                               | 1708 ±5   | 534 ±158                                  |
| Luc-22.5               | 139 ±0                  | 287 ±6                  | 47 ±2                                 | 1554 ±3                                | 0.0038 ±0.0002                       | 250 ±11                                  | 226 ±20                                | 1555 ±3   | 163 ±20                                   |
| <b>BI cave</b>         |                         |                         |                                       |  |                                      |  |  |   |   |
| BI-1.5-.56 mm          | 608 ±27                 | 797 ±16                 | 49 ±2                                 | -288.5 ±2.5                            | 0.00039 ±0.00002                     | 59 ±3                                    | 54 ±5                                  | -289 ±2   | -9 ±5                                     |
| BI-1.5-.44 mm          | 6492 ±32                | 201 ±4                  | 630 ±14                               | -295.8 ±1.8                            | 0.00019 ±0.00001                     | 184 ±2                                   | 182 ±2                                 | -296 ±2   | 120 ±2                                    |
| BI-1.5-.37 mm          | 10036 ±47               | 616 ±12                 | 392 ±9                                | -290.2 ±2.3                            | 0.00146 ±0.00001                     | 224 ±2                                   | 222 ±3                                 | -290 ±2   | 159 ±3                                    |
| BI-1.5-.31 mm          | 8347 ±31                | 10930 ±219              | 2.0 ±1                                | -295.1 ±1.4                            | 0.00019 ±0.00002                     | 247 ±3                                   | 193 ±38                                | -295 ±1   | 130 ±38                                   |
| BI-1.5-.26 mm          | 7424 ±27                | 1633 ±33                | 15.6 ±3                               | -294.3 ±1.5                            | 0.00208 ±0.00002                     | 321 ±3                                   | 312 ±7                                 | -295 ±2   | 249 ±7                                    |
| BI-1.5-.16 mm          | 8318 ±31                | 385 ±8                  | 1052 ±33                              | -295.2 ±2.0                            | 0.00295 ±0.00002                     | 458 ±4                                   | 456 ±4                                 | -296 ±2   | 393 ±4                                    |
| BI-1.5-.10 mm          | 9499 ±41                | 551 ±11                 | 961 ±21                               | -290.9 ±1.5                            | 0.00338 ±0.00002                     | 521 ±4                                   | 519 ±4                                 | -291 ±2   | 456 ±4                                    |
| BI-1.5-.0 mm           | 8128 ±33                | 649 ±13                 | 884 ±18                               | -290.2 ±1.9                            | 0.00428 ±0.00002                     | 660 ±4                                   | 657 ±5                                 | -291 ±2   | 594 ±5                                    |

U decay constants:  $\lambda_{238} = 1.55125 \times 10^{-10}$  (Jaffey et al., 1971) and  $\lambda_{235} = 2.82206 \times 10^{-6}$  (Cheng et al., 2013). Th decay constant:  $\lambda_{230} = 9.1705 \times 10^{-6}$  (Cheng et al., 2013).

$\delta^{230}\text{Th} = \left( \frac{^{230}\text{Th}/^{232}\text{Th}}{^{230}\text{Th}/^{232}\text{Th}} - 1 \right) \times 1000$ .

\*\*  $\delta^{230}\text{Th}_{\text{true}}$  was calculated based on  $^{230}\text{Th}$  age (T), i.e.,  $\delta^{230}\text{Th}_{\text{true}} = \delta^{230}\text{Th}_{\text{measured}} \times e^{2.306T}$ .

Corrected  $^{230}\text{Th}$  ages assume the initial  $^{230}\text{Th}/^{232}\text{Th}$  atomic ratio of  $4.4 \pm 2.2 \times 10^{-6}$ . Those are the values for a material at secular equilibrium, with the bulk earth  $^{230}\text{Th}/^{232}\text{Th}$  value of 3.8. The errors are arbitrarily assumed to be 50%.

\*\*\*B.P. stands for "Before Present" where the "Present" is defined as the year 1950 A.D.

1194  
1195

| Pot au Feu cave |                        |                                      |                                     |                                      |                                       |  |                 |           |   |  |
|-----------------|------------------------|--------------------------------------|-------------------------------------|--------------------------------------|---------------------------------------|--|-----------------|-----------|---|--|
| Sample          | $^{238}\text{U}$ (ppb) | $^{230}\text{Th}/^{238}\text{U}$ (a) | $^{231}\text{U}/^{238}\text{U}$ (a) | $^{232}\text{Th}/^{238}\text{U}$ (a) | $^{230}\text{Th}/^{232}\text{Th}$ (a) | $^{230}\text{Th}$ Age (yr) uncorrected | Age (yr BP) (b) | error     | $^{234}\text{U}/^{238}\text{U}$ Initial (c) |  |
| CT-PP 7.5       | 109                    | 0.022                                | 1.570                               | 0.0084                               | 2.6                                   | 1508                                   | 746             | $\pm 193$ | 1.572                                       |  |
| CT-PP 47        | NR                     | 0.013                                | 1.563                               | 0.0017                               | 7.3                                   | 884                                    | 733             | $\pm 79$  | 1.565                                       |  |
| CT-PP 95        | NR                     | 0.014                                | 1.580                               | 0.0015                               | 9.1                                   | 956                                    | 822             | $\pm 82$  | 1.581                                       |  |
| CT-PP 205       | 95                     | 0.019                                | 1.565                               | 0.0017                               | 11.0                                  | 1330                                   | 1176            | $\pm 68$  | 1.567                                       |  |
| CT-PP 335       | NR                     | 0.030                                | 1.533                               | 0.0051                               | 5.8                                   | 2117                                   | 1652            | $\pm 253$ | 1.536                                       |  |
| CT-PP 400       | 131                    | 0.029                                | 1.533                               | 0.0033                               | 8.6                                   | 2041                                   | 1739            | $\pm 140$ | 1.535                                       |  |
| CT-PP 510       | NR                     | 0.033                                | 1.534                               | 0.0046                               | 7.1                                   | 2347                                   | 1934            | $\pm 145$ | 1.537                                       |  |
| CT-PP 640       | 103                    | 0.036                                | 1.600                               | 0.0052                               | 7.1                                   | 2503                                   | 2060            | $\pm 146$ | 1.604                                       |  |
| CT-PP 740       | 109                    | 0.022                                | 1.570                               | 0.0084                               | 2.6                                   | 1508                                   | 2221            | $\pm 237$ | 1.572                                       |  |
| CT-PP 790       | NR                     | 0.013                                | 1.563                               | 0.0017                               | 7.3                                   | 884                                    | 2099            | $\pm 463$ | 1.565                                       |  |

(a) Activity ratios determined after Hellstrom (2003) using the decay constants of (Cheng et al., 2000)

(b) Age in kyr before present corrected for initial  $^{230}\text{Th}$  using eqn. 1 of (Hellstrom, 2006) and  $[\text{Th}/^{232}\text{Th}]$  of  $0.9 \pm 0.4$

(c) Initial  $[\text{Th}/^{238}\text{U}]$  calculated using corrected age

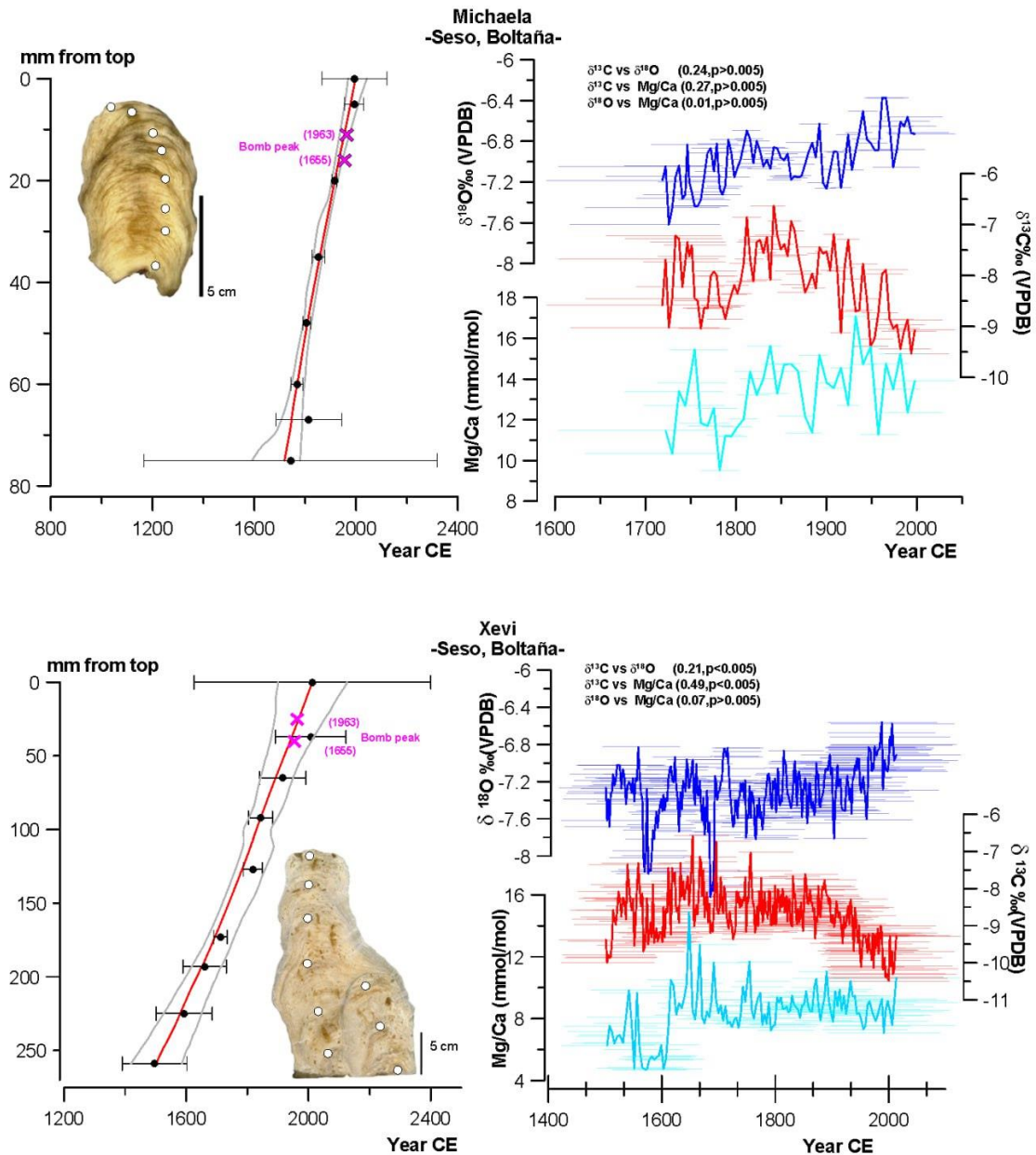
1196  
1197  
1198  
1199

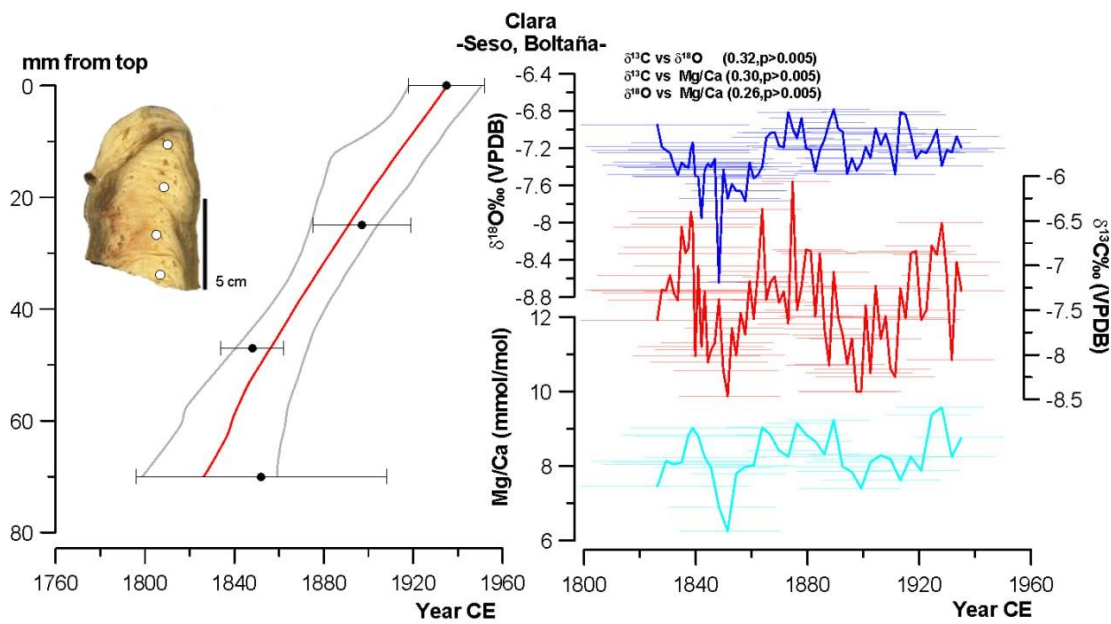
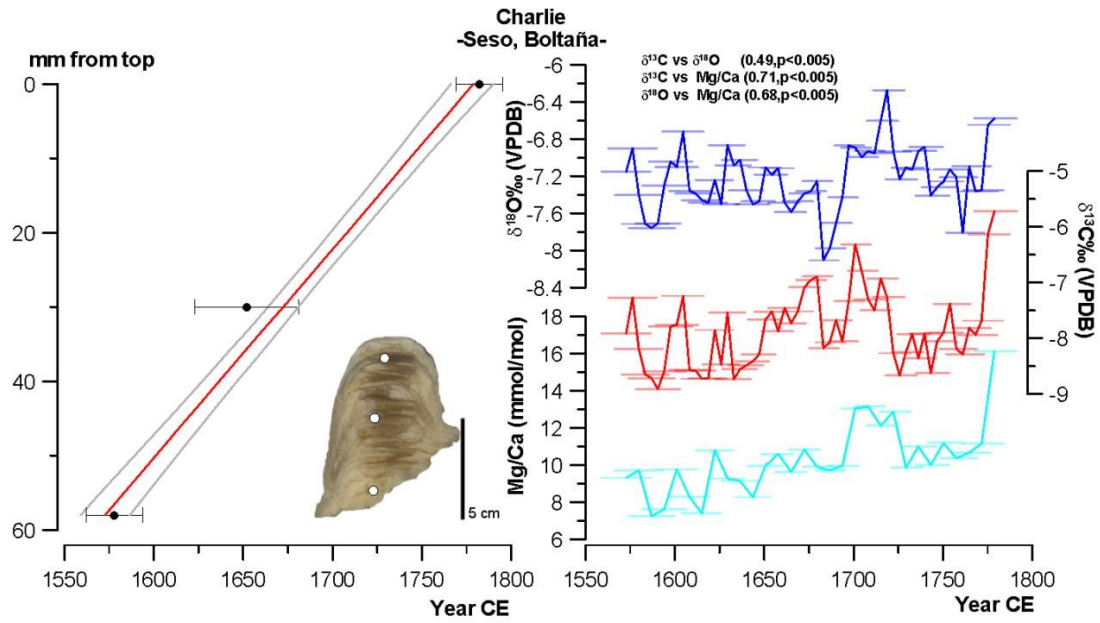
1200

1201 **Appendix A**

1202 **Figure A1.** Polished slabs, age-depth model using StalAge (left) and proxy profiles versus age (right) for the stalagmites used in this study arranged by cave (a. Seso, b. Las Gloces, c. B1, and d. Pot au Feu caves).  
1203 the stalagmites used in this study arranged by cave (a. Seso, b. Las Gloces, c. B1, and d. Pot au Feu caves).  
1204 Correlation coefficients among the three proxies are indicated based on Pearson correlation. Horizontal  
1205 lines represent the age error for every data point, following StalAge uncertainty.

1206 a- Seso cave





1207

1208

1209

1210

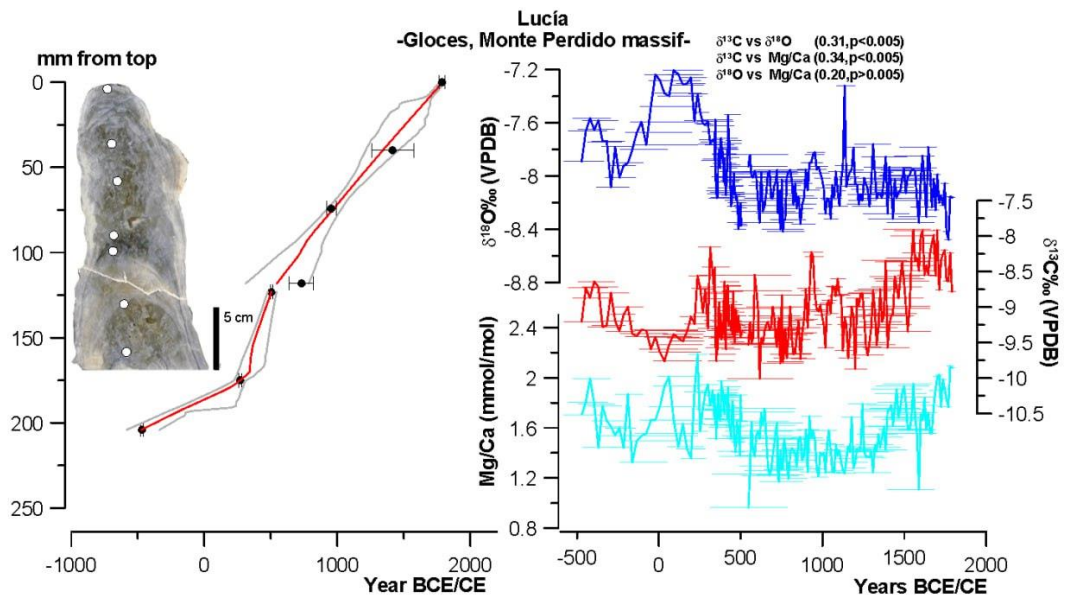
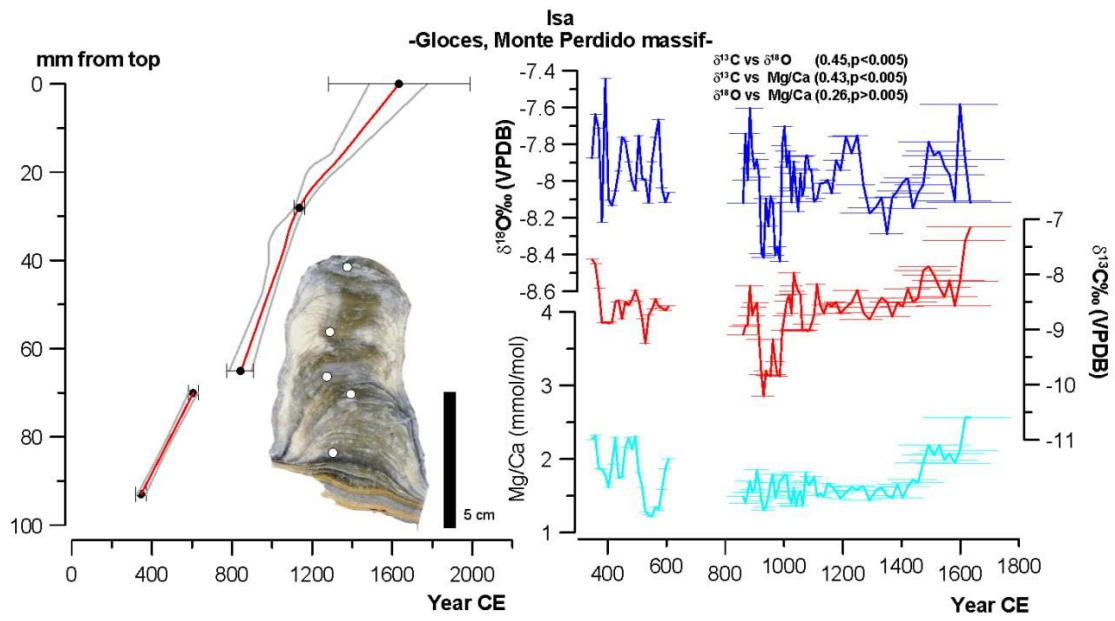
1211

1212

1213

1214

1215



1217

1218

1219

1220

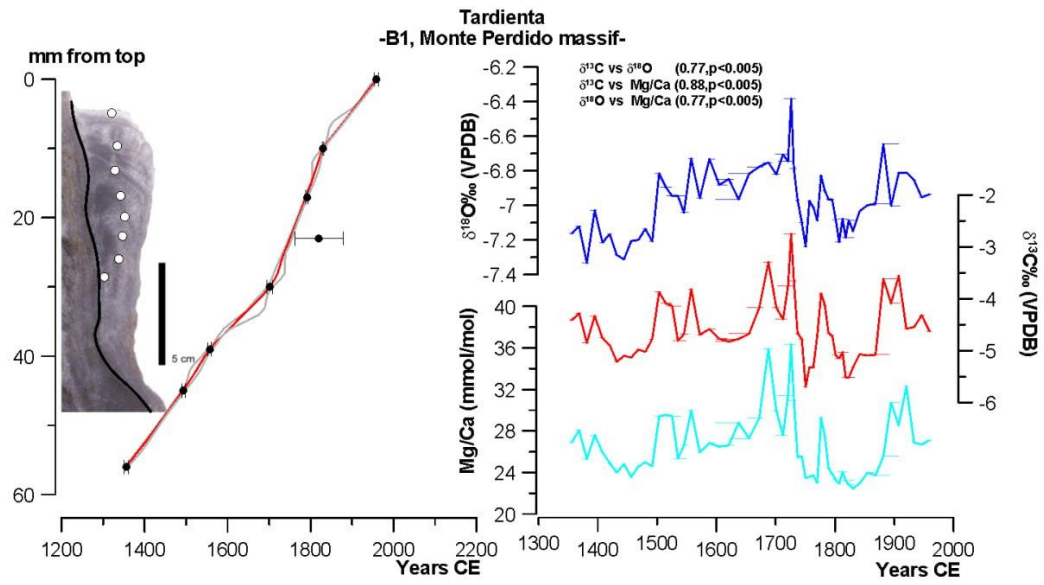
1221

1222

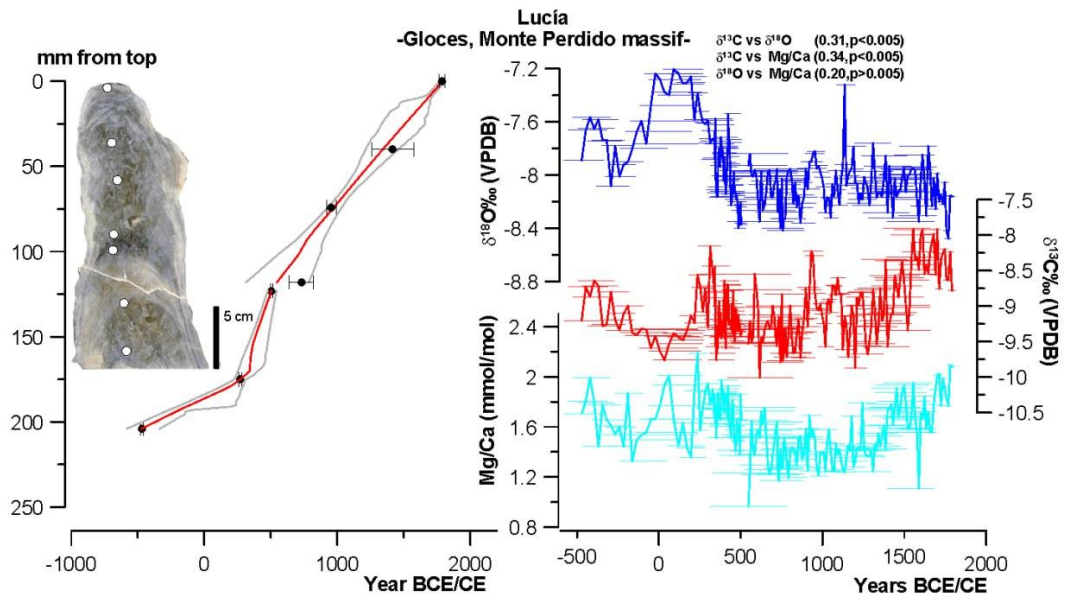
1223

1224

1225 c. B1 cave



1226 d. Pot au Feu cave



1227

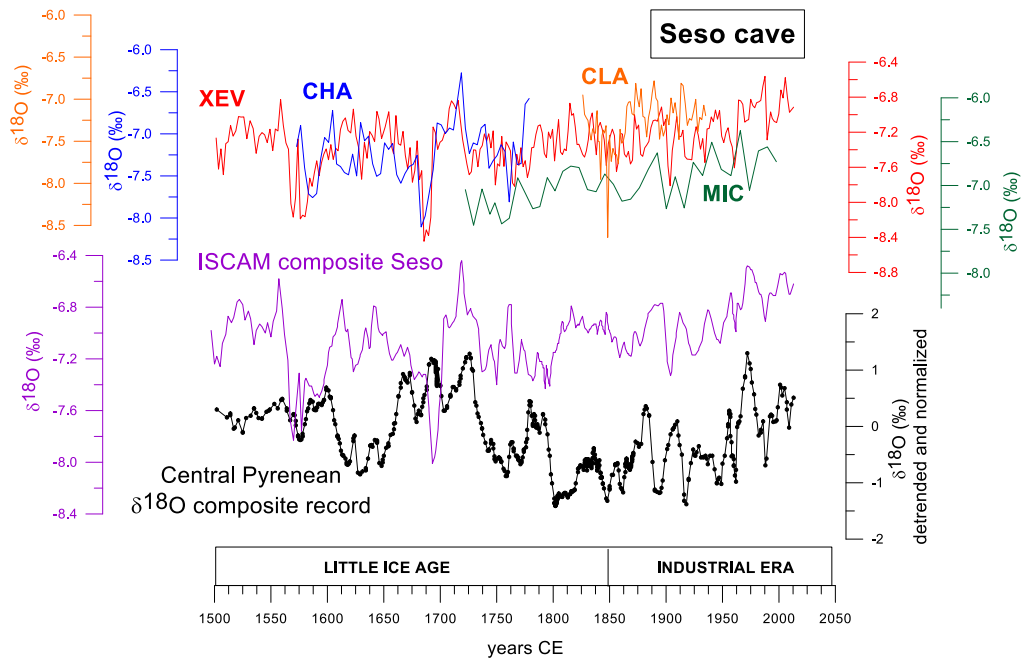
1228



1229

1230 **Figure A2.** Construction of the composite  $\delta^{18}\text{O}$  record for Seso cave. In the upper graph, the individual  
1231  $\delta^{18}\text{O}$  profiles of the four Seso stalagmites are presented, using their StalAge models (XEV in red, CHA in  
1232 blue, CLA in orange and MIC in green). Some records overlap (mostly between XEV and CHA and XEV  
1233 and MIC). The composite  $\delta^{18}\text{O}$  record for Seso cave is shown in purple on the same y-axis as the individual  
1234 curves. The Central Pyrenees  $\delta^{18}\text{O}$  composite record is shown at the bottom of the graph.

1235

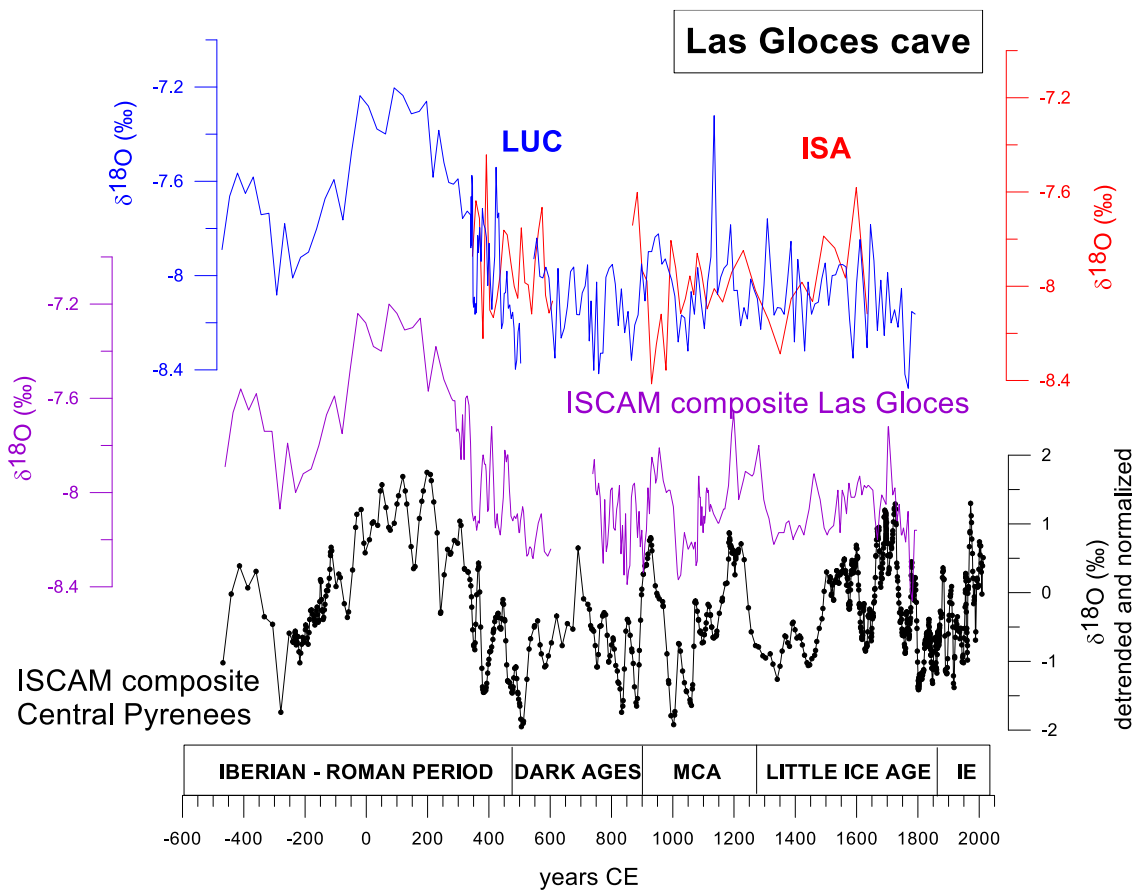


1236

1237

1238 **Figure A3.** Construction of the composite  $\delta^{18}\text{O}$  record for Las Gloces cave. In the upper graph, the  $\delta^{18}\text{O}$   
1239 profiles of the two Las Gloces stalagmites are presented, using their StalAge models (ISA in red and LUC  
1240 in blue). The composite  $\delta^{18}\text{O}$  record for this cave is shown in purple curve on the same y-axis as the  
1241 individual curves. The Central Pyrenees  $\delta^{18}\text{O}$  composite record is shown at the bottom of the graph. MCA:  
1242 Medieval Climate Anomaly, IE: Industrial Era.

1243

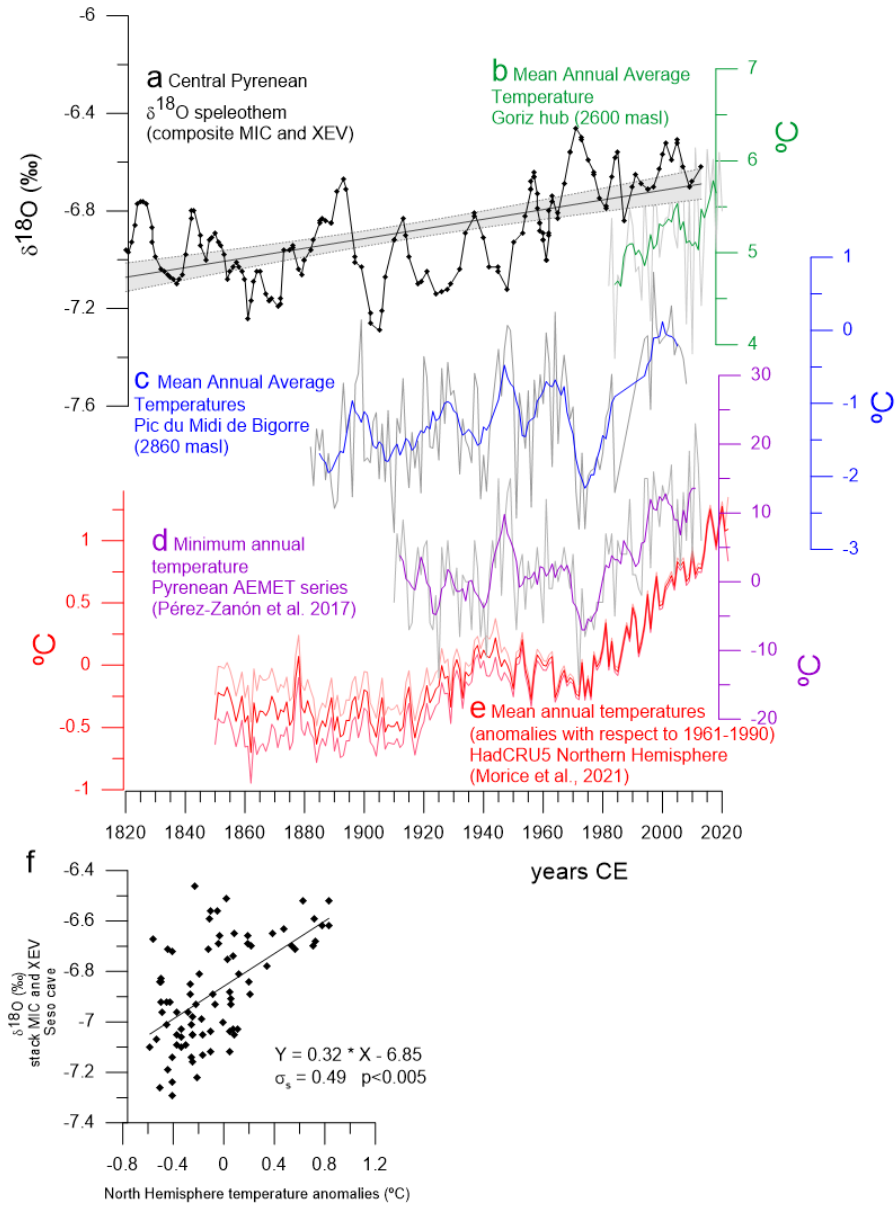


1244

1245

1246

1247 **Figure A4.** Correlation of (a) composite  $\delta^{18}\text{O}$  record from MIC and XEV stalagmites with instrumental  
 1248 temperature records at local, regional and global levels. (b) Mean Annual Average Temperature (MAAT)  
 1249 from Goriz hub (AEMET data); (c) MAAT from Pic du Midi de Bigorre (Bücher and Dessens, 1991;  
 1250 Dessens and Bücher, 1995); (d) Minimum Annual Temperature from the Pyrenees from AEMET series  
 1251 (Pérez-Zanón et al., 2017) and (e) MAAT anomalies (respect to 1961-1990 years) using the HadCRUT  
 1252 5.0.1.0. dataset (Morice et al., 2021). At the bottom, f)  $\delta^{18}\text{O}$  values of the Pyrenees composite record (in a)  
 1253 compared to North Hemisphere mean annual temperatures (in e) showing a significant correlation.



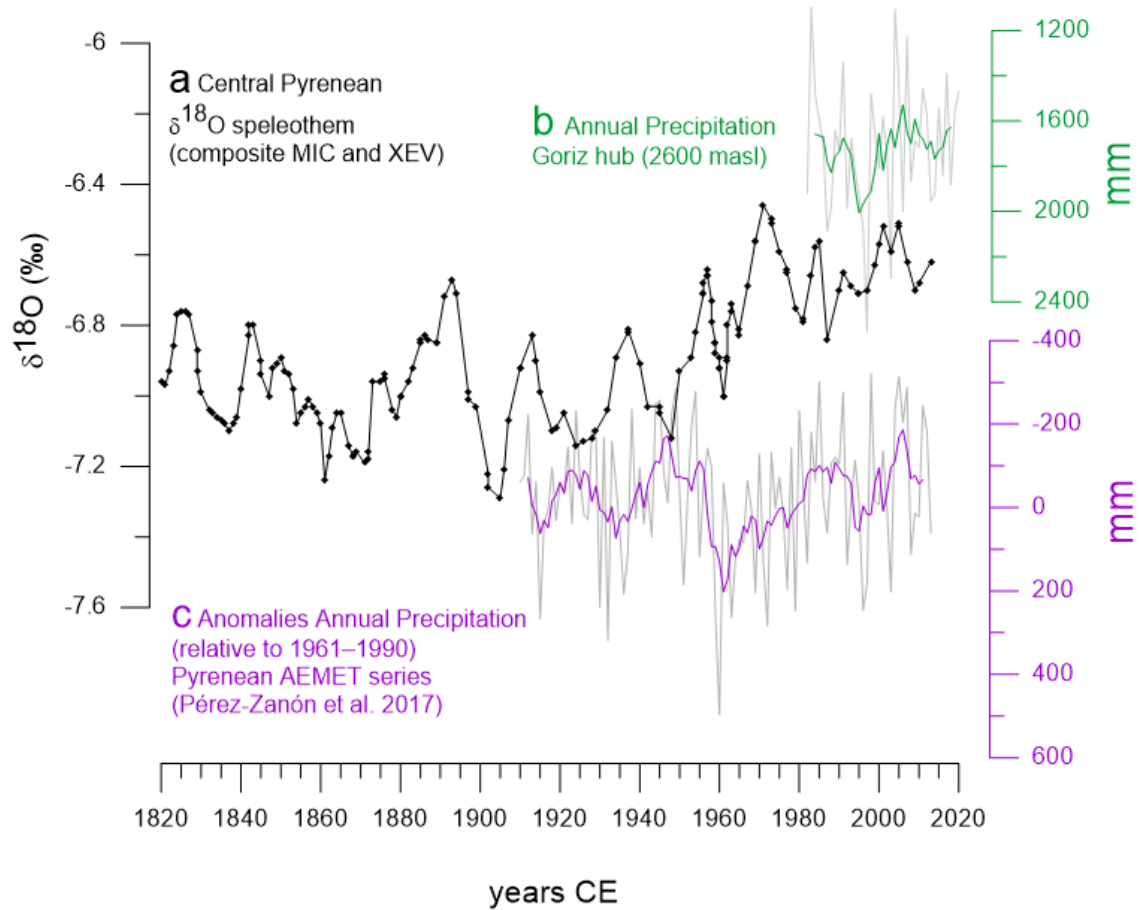
1254

1255

1256

1257 **Figure A5.** Correlation of (a) composite  $\delta^{18}\text{O}$  record from MIC and XEV stalagmites with instrumental  
1258 precipitation records at regional levels. (b) Annual precipitation from Goriz hub (AEMET data) and (c)  
1259 Precipitation anomalies from the Pyrenees from AEMET series (respect to 1961-1990 years) (Bücher and  
1260 Dessens, 1991; Dessens and Bücher, 1995). No significant correlation is observed.

1261



1262

1263